Theoretical and Observational Tests of Scalarization

by

Ekrem Seyfi Demirboğa

A Dissertation Submitted to the
Graduate School of Sciences and Engineering
in Partial Fulfillment of the Requirements for
the Degree of

Master of Science

in

Physics

KOÇ ÜNİVERSİTESİ

July 13, 2023

Theoretical and Observational Tests of Scalarization

Koç University

Graduate School of Sciences and Engineering

This is to certify that I have examined this copy of a master's thesis by

Ekrem Seyfi Demirboğa

and have found that it is complete and satisfactory in all respects,

and that any and all revisions required by the final

examining committee have been made.

Committee Members:

Asst. Prof. Fethi Mübin Ramazanoğlu

Prof. Tekin Dereli

Prof. Emre Onur Kahya

Date:

İlm, bir kîl-ü kaal imiş ancak.

Fuzuli

ABSTRACT

Theoretical and Observational Tests of Scalarization
Ekrem Seyfi Demirboğa
Master of Science in Physics
July 13, 2023

Scalarization is a phenomenon that occurs in certain modified gravity theories where the scalar field spontaneously grows in the vicinity of compact objects. This allows the theory to closely resemble general relativity in weakly gravitating environments and deviate from it in systems where gravity is strong. At the linear level, it manifests as a Tachyonic instability. This thesis will study this phenomenon using theoretical and observational tools. The first part of the thesis will be based on observations where we will introduce a technique that can test scalarization using neutron star mass and radius measurements. More specifically, we will show that the theory parameters of two scalarization models, the scalar-Gauss-Bonnet Model (sGB) and the Damour and Esposito-Farèse (DEF) model, can be constrained using neutron star mass-radius data. We will show that this method successfully constrains the sGB model, but the same is not always true for the DEF model. In the second part, we will examine theoretical tools to test ideas inspired by scalarization. Namely, we will show that a straightforward generalization of scalarization to vectors, named vectorization, suffers from not only tachyonic instability but also ghost instability. This leads to the likely conclusion that such generalizations are unphysical, which enables us to rule out most such theories by purely theoretical means.

ÖZETÇE

Yüksek Lisans Tez Başlığı
Ekrem Seyfi Demirboğa
Fizik, Yüksek Lisans
13 Temmuz 2023

Skalarizasyon, skaler alanın kompakt nesnelerin yakınında kendiliğinden büyüdüğü, belirli değiştirilmiş yerçekimi teorilerinde meydana gelen bir olgudur. Bu, teorinin zayıf yerçekimi olan ortamlarda Genel Göreliliğe çok benzemesine ve yerçekiminin güçlü olduğu sistemlerde ondan sapmasına izin verir. Doğrusal seviyede, takyonik kararsızlık olarak kendini gösterir. Bu tezde, bu fenomeni teorik ve gözlemsel araçlar ışığında iki kısımda inceleyeceğiz. Tezin ilk bölümü, nötron yıldızı kütle ve yarıçap ölçümlerini kullanarak skalarizasyonu test edebilen gözlemsel bir tekniğe dayanacaktır. Özellikle, iki skalarizasyon modelinin, skaler-Gauss-Bonnet Modeli (sGB) ve Damour ve Esposito-Farèse (DEF) modelinin teori parametrelerinin, nötron yıldızı kütle yarıçapı verileri kullanılarak kısıtlanabileceğini göstereceğiz. Bu yöntemin sGB modeline kısıtlamalar getirmede başarılı olduğunu, ancak aynı durum DEF modeli için her zaman geçerli olmadığını göstereceğiz. İkinci bölümde ise, skalerizasyondan ilham almış bazı fikirleri test etmek teorik araçlar geliştirip, inceleyeceğiz. Diğer bir değişle, skalarizasyonun vektörlere basit bir genelleştirilmesinin, vektörizasyonun, sadece takiyonik kararsızlıktan değil, aynı zamanda hayalet kararsızlıktan da muzdarip olduğunu göstereceğiz.Dolayısıyla, bu gibi genellemelerin fiziksel olmadığı ve bu tür teorilerin çoğunu sadece teorik yollarla eleyebildiğimiz sonucuna varabiliyoruz.

ACKNOWLEDGMENTS

I would like to thank my supervisor, Fethi Mübin Ramazanoğlu, for his guidance and mentorship throughout my academic life. His expertise and valuable insights have been instrumental in shaping the direction of my research and enhancing its quality.

I would also like to extend my heartfelt appreciation to my parents and my sister for their constant encouragement and unwavering belief in my abilities; and to my friends, as their friendship has made the challenging times more manageable and the joyous moments more memorable.

Throughout my life, I have crossed paths with numerous remarkable individuals who have played an invaluable role in shaping the person I have become today. I cannot explicitly write all the names, but I am grateful I had known them.

I should also thank the Koç University Administration for their policies regarding the grad school and dormitories last year, which showed the value the university placed on its students and led me to finish my master's degree in less than a year.

TABLE OF CONTENTS

LIST OF TABLES

LIST OF FIGURES

ABBREVIATIONS

GR	General Relativity
DEF	Damour and Esposito-Farèse
sGB	Scalar-Gauss-Bonnet
NS	Neutron star
EOS	Equation of state
TOV	Tolman Oppenheimer Volkoff
LIGO	Laser Interferometer Gravitational-Wave Observatory
KAGRA	Kamioka Gravitational Wave Detector.

Chapter 1

INTRODUCTION

Einstein's General Theory of Relativity (GR) stands as one of the most elegant and successful theories in physics. It has achieved remarkable success by providing explanations for previously unexplained observations and making astounding predictions that have subsequently been confirmed. Among these successful observations and predictions are the existence of gravitational waves [1], and all the solar system tests performed so far [2, 3]. Furthermore, GR has demonstrated consistency with all direct gravitational wave observations conducted in collaboration with LIGO, Virgo, and KAGRA [4, 5].

In view of various theoretical and observational factors, the pursuit of alternative theories of gravity remains valuable despite the achievements of GR. First, and perhaps the most important example, is the fact that GR is incompatible with Quantum Mechanics [6, 7]. Even though both of these theories are proven to be very successful on their own, one faces some inconsistencies where the two theories intersect. Therefore, one can think of the existence of a complete quantum gravity theory where the classical limit would be a modified version of GR. This is indeed the motivation behind some of the alternative gravity models [8, 9]. Second, GR fails to explain some phenomenon in cosmology without introducing entities like *dark matter* or *dark energy* whose true origin is not well understood. Finally, there is an argument that numerous experiments examine the fundamental principles of GR, not the theory itself, which gives room to modify the theory.

However, due to Lovelock's Theorem [10], we can not freely modify the field equations if we want a physical theory free from instabilities. The theorem states that if we want to modify GR, things we can do are the following:

- Adding additional fields (e.g., scalar-tensor, vector-tensor)
- Adding more dimensions (e.g., Kaluza–Klein theory)
- Adding more than second derivatives of the metric to the action (e.g., Gauss-Bonnet theory)
- Giving up locality (e.g., Non-local gravity)
- Emergence (e.g., entropic force)

The first and third items above, namely scalar-tensor, vector-tensor, and Gauss-Bonnet theories, will be the main focus of this thesis. The solar system is a perfect laboratory for testing the weak field limit of such theories, and with the observation of the gravitational waves, it is now possible to test them in the strong field limit as well [4, 11]. Given the success of GR in the weak field limit, the most promising theories are the ones that mimic GR in the weak field limit and largely deviate from GR in the strong curvature regime. The mechanisms that ensure that are called *screening mechanisms*, and the most famous example is the *spontenous scalarization* or often referred to as *scalarization* introduced in Ref. [9] which will be the central theme throughout the thesis.

Lately, there has been a notable increase in interest surrounding the exploration of gravity's characteristics in the regime of strong curvature due to the aforementioned reasons. Consequently, numerous alternative theories were proposed in the literature [9, 12–14]. Therefore, it is essential to constrain these newly emerging theories or perhaps rule them out either with purely theoretical considerations or using observational data. The rest of the thesis is arranged as follows: In the following Chapter, we will lay out the theoretical preliminaries and give an introduction to the *scalarization*; in Chapter. 3, we will show that using neutron star mass-radius measurements is effective in constraining some scalarization models and providing bounds, yet this is not the case in general; that is, this methodology might fail in specific models. Then, in Chapter. 4, we will study the theoretical tests of scalarization and show that vectorization, a direct generalization of scalarization, contains instabilities and, therefore, due to theoretical considerations only, can not be a physical theory. Finally, in Chapter. 5 We will give a summary of the thesis and discuss the possible extensions. Unless stated otherwise, we will use the units where $c = G = 1$ and adopt the metric signature $(-,+,+,+)$ for the rest of the thesis.

Chapter 2

SCALARIZATION

In recent years, there has been a significant increase in observations to probe the physics beyond GR and Standard Model, see, e.g., Refs. [13, 15, 16]. One of the exciting possibilities is the existence of a new fundamental field, e.g., a scalar field. However, problems arise when one considers the success of GR in the weak field limit. In other words, even if such fields exist, they must behave such a way that the theory should be identical to GR when gravity is weak. In the case of a scalar field, such behavior is shown to exist in some alternative gravity theories [9]. The mechanism ensuring this is called *scalarization* and later generalized to other fields [17, 18]. Scalarization, sometimes referred to as spontaneous scalarization, is a phenomenon that occurs in certain modified gravity theories in which the scalar field grows in the vicinity of compact objects such as black holes or neutron stars. Here we will give a brief introduction to the idea of scalarization and lay out the theoretical preliminaries. For more details on the subject, see Ref. [11].

2.1 Theoretical background

Let us examine a simpler model to understand better the mechanism behind the *scalarization*. Assume a real scalar field φ in a Minkowski spacetime whose Lagrangian is given by

$$\mathcal{L} = \frac{1}{2}\eta^{\mu\nu}\partial_\mu\varphi\partial_\nu\varphi + V(\varphi), \tag{2.1}$$

which results in the following equation of motion for the scalar field

$$\Box_\eta\varphi = \frac{\mathrm{d}V(\varphi)}{\mathrm{d}\varphi}\,, \tag{2.2}$$

where $\eta_{\mu\nu}$ is the metric of the flat spacetime and $\Box_\eta \equiv \eta^{\mu\nu}\partial_\mu\partial_\nu$ is the d'Alembertian in Minkowski spacetime. A specific choice of $V(\varphi) = \frac{1}{2}m_\varphi^2\varphi^2$ reduces to the Klein-

Gordon equation with Fourier modes

$$\varphi(x^\mu) = e^{ik_\mu x^\mu} = e^{i[-\omega t + \mathbf{k}\cdot\mathbf{x}]} \,, \tag{2.3}$$

where m_φ is the bare mass of the scalar field, ω is the frequency and $\mathbf{k}$ is the wave vector. Then, the corresponding dispersion relation is given by

$$\omega^2 = \mathbf{k}^2 + m_\varphi^2 \,, \tag{2.4}$$

which is nothing but relativistic energy-momentum relation. In the case of $m_\varphi^2 > 0$, the modes (2.3) oscillate in time. Instead, in the case of $m_\varphi^2 < 0$, the modes with the small wave vector admit imaginary frequency and, as a result, exponentially grow or decay. This is called *tachyonic instability*. A more detailed analysis of the types of instabilities will be discussed in section Sec. 4.1.

Now assume a potential given by

$$V(\varphi) = \frac{1}{2}m_\varphi^2\varphi^2 + \frac{1}{4}\lambda\varphi^4. \tag{2.5}$$

Then, the scalar field obeys the following equation of motion

$$\Box_\eta\varphi = m_\varphi^2\varphi + \lambda\varphi^3. \tag{2.6}$$

It is trivial that $\varphi = 0$ solves this equation. Therefore, we can linearize this equation around $\varphi = 0$. Considering small perturbations $\delta\varphi$, linearized equation satisfies

$$\Box_\eta\delta\varphi \approx m_\varphi^2\delta\varphi, \tag{2.7}$$

where again, by the same logic as in the Klein-Gordon case, $m_\varphi^2 < 0$ results in tachyonic instability. This might seem like a pathology for the theory at first sight, but this is not necessarily true. Because as the field φ grows, nonlinear terms $\lambda\varphi^3$ in the Eq. (2.6) becomes important, and the Eq. (2.7) will no longer be valid. In fact, it will be this nonlinear term that will determine the endpoint of the stability. For example, if we take $\lambda > 0$, the potential (2.5) will take the well-known "Mexican hat" shape as in Fig. 2.1. Then, Eq.(2.6) admits a second constant φ solution at the local minimum of the potential. Therefore, tachyonic instability drives the system from the local maximum where $\varphi = 0$ to the stable local minimum where $\varphi = \varphi_0$.

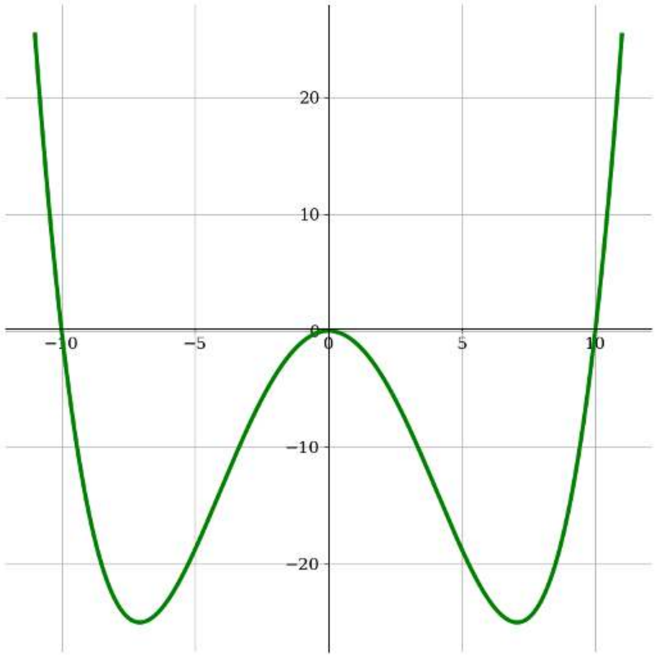

Figure 2.1: Mexican hat potential. The shape of the potential given in Eq. (2.5) for $\lambda > 0$.

This can also be seen as a phase transition of the system and, therefore, sometimes called *tachyon condensation* [11].

This mechanism can also be generalized to a more general metric $g_{\mu\nu}$. Then the Eq. (2.7) simply becomes

$$\Box_g \delta\varphi \approx m_\varphi^2 \delta\varphi, \tag{2.8}$$

where $\Box_g = g^{\mu\nu}\nabla_\mu\nabla_\nu$ and ∇_μ is the covariant derivative. In particular, let us take a static, spherically symmetric background,

$$\mathrm{d}s^2 = -e^{2\alpha(r)}\,\mathrm{d}t^2 + e^{2\beta(r)}\,\mathrm{d}r^2 + r^2\,\mathrm{d}\Omega^2, \tag{2.9}$$

where $\mathrm{d}\Omega^2 = \mathrm{d}\theta^2 + \sin^2\theta\,\mathrm{d}\phi^2$. Then, we can decompose the scalar perturbations into spherical harmonics and the solutions can be written as a combination of the modes

$$\delta\varphi_{\omega lm} = \frac{\psi_{lm}(r)}{r} Y_{lm}(\theta,\phi) e^{-i\omega t}. \tag{2.10}$$

Plugging this into Eq. (2.8) results in a Schrödinger like equation for $\psi_{lm}(r)$

$$\left(-\frac{\mathrm{d}^2}{\mathrm{d}x^2}+V_{\mathrm{eff}}(r)\right)\psi_{lm}(r)=\omega^2\psi_{lm}(r)\,, \tag{2.11}$$

where we defined $x\equiv\int_0^r e^{\beta(r')-\alpha(r')}\,\mathrm{d}r$ and effective potential V_{eff} is given by

$$V_{\mathrm{eff}}(r)=\frac{e^{2(\alpha-\beta)}}{r}\frac{\mathrm{d}(\alpha-\beta)}{\mathrm{d}r}+\frac{l(l+1)}{r^2}e^{2\alpha}+m_\varphi^2e^{2\alpha}\,. \tag{2.12}$$

If $m_\varphi<0$ and, as a result, the last term is sufficiently negative, the operator $-\frac{\mathrm{d}^2}{\mathrm{d}x^2}+V_{\mathrm{eff}}(r)$ may have negative eigenvalues, i.e., $\omega^2<0$, which implies the existence of tachyonic instability. In other words, we can conclude that the condition

$$\int V_{\mathrm{eff}}(r)\,\mathrm{d}x\leq 0, \tag{2.13}$$

is sufficient but not necessary for having a tachyon in our system.

In summary, the mechanism behind the scalarization relies on the fact that governing equations of motions contain tachyonic instabilities, which, in turn, depend on the metric of spacetime. Perturbation analysis of these equations to the linear order is helpful in determining the onset of scalarization. However, the endpoint of the instability is determined by the nonlinear terms in the potential.

2.2 Examples of scalarization

In the previous section, we considered a scalar field with a bare mass m_φ and studied the cases where $m_\varphi^2<0$, which amounts to having an imaginary bare mass. Typically, this is not something that one would expect; therefore, one might think that having instability, in this case, is no surprise. However, when we include the gravity to the picture, i.e., when we add Einstein-Hilbert term coupled to the scalar field, e.g., φ^2R to the Lagrangian in (2.1), the resulting equations for the scalar field will contain terms like $2\varphi R$. In other words, non-minimal coupling to gravity will act as an effective mass for the scalar field as $m_{\mathrm{eff}}=m_\varphi+2R$. Therefore, even if we take the bare mass of the scalar field zero, $m_\varphi=0$, there will be nonzero effective mass in the equations governing the dynamics of the scalar field, which can, in principle, trigger scalarization. Here, we will provide two prominent examples of scalarization in gravity theories, namely, the Damour and Esposito-Farèse model [9] and Scalar-Gauss-Bonnet model [14, 19, 20]

2.2.1 Damour and Esposito-Farèse model

The idea of *spontaneous scalarization* was first introduced by Damour and Esposito-Farèse (DEF) where they consider the action [9]

$$\frac{1}{16\pi}\int \mathrm{d}^4x\sqrt{-g}\left[R-2g^{\mu\nu}\nabla_\mu\varphi\nabla_\nu\varphi\right]+S_\mathrm{m}\left[\psi_\mathrm{m};\mathcal{A}(\varphi)g_{\mu\nu}\right], \tag{2.14}$$

where S_m is the matter action and ψ_m represents any matter field. Here, the scalar field is minimally coupled to gravity, and the matter field is coupled to some conformally scaled metric $\tilde{g}_{\mu\nu}=\mathcal{A}(\varphi)g_{\mu\nu}$. This formulation in Action (2.14) is in the so-called Einstein frame, and the metric with the tilde, $\tilde{g}_{\mu\nu}$, is said to be Jordan Frame metric. If we were to write the Action (2.14) in the Jordan frame, we would obtain a non-minimal coupling to gravity and a minimal coupling to matter fields. Writing the equations of motion for the scalar field from the Action (2.14) gives

$$\Box_g\varphi = -4\pi\frac{\mathrm{d}(\ln\mathcal{A})}{\mathrm{d}\varphi}T, \tag{2.15}$$

where T is the trace of the stress-energy tensor in Einstein frame, $T^{\mu\nu}=2-(g)^{1/2}(\delta S_\mathrm{m}/\delta g_{\mu\nu})$. Now let us rewrite the equation for the scalar field in a different form as

$$\Box_g\varphi = -8\pi\mathcal{A}^4\frac{\mathrm{d}(\ln\mathcal{A})}{\mathrm{d}\varphi^2}\tilde{T}\varphi. \tag{2.16}$$

where we used the trace of the stress-energy tensor in Jordan frame $\tilde{T}$. Similar to our logic in Sec. 2.1, we linearize this equation to get,

$$\Box_g\varphi \approx -8\pi\left[\mathcal{A}^4\frac{\mathrm{d}(\ln\mathcal{A})}{\mathrm{d}\varphi^2}\right]_{\varphi=0}\tilde{T}\varphi \equiv m^2_\mathrm{eff}\,\varphi. \tag{2.17}$$

where we defined a spacetime-dependent effective mass term, m^2_eff, which can take negative values as well. If that is the case, small perturbations around $\varphi=0$ can trigger tachyonic instability, i.e., exponentially growing modes. This instability, however, can be quenched due to nonlinear terms becoming dominant, and the resulting configuration can be stable, i.e., a scalarized solution.

Let us examine a neutron star in this theory as an example. We model the matter as perfect fluid, hence $\tilde{T} = -\tilde{\rho} + 3\tilde{p}$. For non-relativistic matter, we have $\tilde{\rho} \gg \tilde{p}$, therefore, $\tilde{T} \approx -\rho < 0$ for a neutron star. If our choice of the coupling function can be expanded as

$$\mathcal{A}(\varphi) = 1 + \beta \frac{\varphi^2}{2} + \ldots, \tag{2.18}$$

where $\beta < 0$, together with the fact $\tilde{T} < 0$, then the effective mass can be negative inside the star, $m^2_{\text{eff}} < 0$ and Eq. (2.17) will have a tachyonic instability and nonlinear terms can quench this instability later on, i.e., the star is scalarized.

Another possibility for having a tachyonic instability is to have $\beta > 0$ and $\tilde{T} > 0$, which is possible in some neutron stars near the core of the star for some equation of state [21–26]. In this case, most of the neutron stars are not expected to scalarize. However, there might be some massive stars in which scalarization can occur.

It may seem that this argument holds for any matter distribution; however, noting that outside the star $\tilde{T} = 0$, therefore, $m_{\text{eff}} = 0$; as well as other factors due to spherical symmetry shows that, only stars with a sufficiently negative effective mass can scalarize [27].

Throughout this thesis, we will consider two choices for the coupling function, which will have a Taylor expansion of the from (2.18)

$$\mathcal{A}(\varphi) = e^{\beta\varphi^2/2} \qquad \textbf{Quadradtic DEF} \tag{2.19}$$

$$\mathcal{A}(\varphi) = \left(\cosh \sqrt{3}\beta\varphi\right)^{1/(3\beta)} \qquad \textbf{Linear DEF} \tag{2.20}$$

where the naming is due to the behavior of the coupling function in the limit $\varphi \to \infty$, i.e., $\ln[\mathcal{A}(\varphi \to \infty)] \sim \varphi^2$ for quadratic DEF and $\ln[\mathcal{A}(\varphi \to \infty)] \sim \varphi$ in the linear DEF model. The quadratic DEF is the most commonly used model in the literature, and it is the one that was originally used in Damour and Esposito-Farèse [9], The linear DEF model is introduced in Mendes and Ortiz [22] with the main motivation of resolving the stability issues arising in some cases as well as some other motivations coming from quantum field theory and renormalization [28].

2.2.2 Scalar-Gauss-Bonnet model

Another model that exhibits scalarizaton is scalar-Gauss-Bonnet Gravity (sGB) with Action [14, 19, 20, 29]

$$S = \frac{1}{16\pi}\int d^4x\left[R - 2g^{\mu\nu}\nabla_\mu\varphi\nabla_\nu\varphi + \frac{\beta_{\rm GB}}{R_0^2}f(\varphi)\mathscr{G}\right], \tag{2.21}$$

where

$$\mathscr{G} = R^{\mu\nu\rho\sigma}R_{\mu\nu\rho\sigma} - 4R^{\mu\nu}R_{\mu\nu} + R^2, \tag{2.22}$$

is the Gauss-Bonnet invariant, $\beta_{\rm GB}$ is the dimensionless parameter of the theory. We also introduced a length scale R_0 to make $\beta_{\rm GB}$ dimensionless, typically chosen to be one solar mass in geometric units[1] [20]. The field equation for the scalar field from the Action (2.21) yields

$$\Box\varphi = -\beta_{\rm GB}\frac{df(\varphi)}{d\varphi}\mathscr{G}. \tag{2.23}$$

After defining an effective mass as $m^2_{\rm eff} \equiv -\beta_{\rm GB}\mathscr{G}\, d^2f(\varphi)/d^2\varphi$ and linearizing we end up with

$$\Box\varphi \approx m^2_{\rm eff}\varphi\,, \tag{2.24}$$

which has same form as the Eq. (2.8) and Eq. (2.17) and therefore some class of coupling function $f(\varphi)$ allow for scalarization. Here we will focus on a specific choice following [20] and follow the notation of [29]

$$\beta_{\rm GB}f(\varphi) = \beta_{\rm GB}\frac{e^{-\sigma\varphi^2} - 1}{2\sigma} \qquad \textbf{sGB model} \tag{2.25}$$

where we named this specific choice *scalar-Gauss-Bonnet (sGB)* model following [29]. Note that the asymptotic behavior is similar to the quadratic DEF model. Additionally, similar to the DEF model, the onset of the scalarization is controlled by the parameter $\beta_{\rm GB}$, however, the end state configuration of the scalar field and the spacetime is determined by the nonlinear terms, which are controlled by σ. We will discuss this further in Chapter 3. Also, it is important to note that in the scalar-Gauss-Bonnet (sGB) model, not only the neutron stars but Blackholes as well can scalarize, which was not the case in DEF [19, 20, 30].

[1] this corresponds to having $R_0 = 1.47664$km

2.3 Beyond scalarization

The *scalarization* mechanism is not limited to scalar fields. The first possible extension is to generalize the idea to vector fields [17]. However, it is also possible to generalize the idea to any tensor fields, p-forms, and even spinors [18, 31, 32]. Here will only consider the vector field case, namely, *vectorization*. Start with the following action [17]

$$S = \frac{1}{16\pi} \int \mathrm{d}^4x \left[R - F^{\mu\nu}F_{\mu\nu} - 2m_V^2 \mathfrak{x}^2 \right] + S_\mathrm{m}\left[\psi_\mathrm{m}; \mathcal{A}(\mathfrak{x}) g_{\mu\nu} \right], \tag{2.26}$$

where $F_{\mu\nu} = \nabla_\mu X_\nu - \nabla_\nu X_\mu$ is the Faraday tensor, $\mathfrak{x} \equiv \sqrt{g^{\mu\nu} X_\mu X_\nu}$, $\mathcal{A}(\mathfrak{x})$ is the conformal factor similar to DEF and sGB, and A_α is the vector field. We also considered a bare mass m_V of the vector field for the sake of completeness which is not necessary for tachyonic instability. It makes it hard for the equation to be tachyonic, as we will see. The field equation from the Action (2.26)

$$\nabla_\alpha F^{\alpha\mu} = \underbrace{\left[m_V^2 - 8\pi \mathcal{A}(\mathfrak{x})^4 \frac{\mathrm{d}\ln \mathcal{A}}{\mathrm{d}\mathfrak{x}} \tilde{T} \right]}_{\equiv m_\mathrm{eff}} X^\mu, \tag{2.27}$$

where the term inside the bracket acts as an effective mass, m_eff. Therefore when the condition $m_\mathrm{eff} < 0$ is satisfied, the vector field will grow exponentially due to tachyonic instability around $X^\mu = 0$, just as in the scalarization case, which we will say vectorization.

One can also write a vector-tensor theory with a Gauss-Bonnet term [11]

$$S = \frac{1}{16\pi} \int \mathrm{d}^4x \left[R - F^{\mu\nu}F_{\mu\nu} + f(\mathfrak{x})\mathcal{G} \right], \tag{2.28}$$

where we can have vectorized black holes. Even though the mechanism seems quite similar to what we have for scalarization, there are some uncertainties regarding the final state of the vectorized solutions due to vectors having 3 degrees of freedom, whereas scalars only have one. Additionally, the neutron star and black hole solutions are qualitatively different in scalar-tensor and vector-tensor theories [11]. Later on Sec. 4, we will see that, there are, in fact, major differences between vectorization and scalarization [33, 34].

Chapter 3

OBSERVATIONAL TESTS OF SCALARIZATION

The observations of compact objects such as black holes and neutron stars shed light on the astrophysics of such systems as well as our understanding of gravity [15, 16, 35]. One of the most powerful tools for these observations is gravitational waves; however, electromagnetic wave observations such as x-ray observations of neutron stars are also improved in recent years [36–38]. One example is the simultaneous measurement of a neutron star's mass and radius [39].

Mass-radius data is proved to be helpful in determining the Equation of State (EOS) of the nuclear matter in neutron stars [39]. The main idea is that changing the EOS changes the neutron star structure and, therefore, the mass-radius diagram predicted by such a model. Then, one can use this data to put constraints on the model's parameters if the deviations are large enough.

Here we will investigate the gravity models that deviate from GR in terms of neutron star structure. In these theories, the TOV equations that determine the structures of stellar objects get modified as well and may result in significant deviations from GR. As we showed in Chapter. 2.1, one of the most compelling examples for such theories are the ones that exhibit *scalarization*. In this scenario, compact objects, like neutron stars, obtain a scalar cloud around them, drastically changing their structure. We will discuss the idea of using mass-radius measurements to constrain these theories and how feasible the idea is.

We will follow the discussions in [29, 40]. The rest of the chapter is organized as follows: In Sec 3.1 we derive the modified TOV equations for the models presented before; in Sec 3.2, we explain how we obtained the theoretically predicted neutron star solutions, the stability of these solutions, and how we assigned likelihood to these models to constrain them using mass-radius data; In Sec 3.3 we present our findings.

3.1 Equations of Motions: TOV framework

We have already introduced the DEF and sGB model Lagrangian in (2.14) and (2.21) respectively and investigated the scalar field's equation of motion. Now, for the sake of completeness, let's present the modified field equations here as well. Starting with the DEF model, we have the following equations of motion

$$R_{\mu\nu} = 8\pi(T_{\mu\nu} - \frac{1}{2}g_{\mu\nu}T) + 2\nabla_\mu\varphi\nabla_\nu\varphi, \tag{3.1}$$

$$\Box_g\varphi = -4\pi\alpha(\varphi)T, \tag{3.2}$$

where we introduced

$$\alpha(\varphi) \equiv \frac{\mathrm{d}(\ln\mathcal{A})}{\mathrm{d}\varphi}. \tag{3.3}$$

We are interested in neutron star solutions; therefore, we make use of the following static, spherically symmetric metric ansatz:

$$\mathrm{d}s^2 = -e^{\nu(r)}\,\mathrm{d}t^2 + \frac{1}{1-\frac{2\mu(r)}{r}} + r^2\,\mathrm{d}\Omega^2. \tag{3.4}$$

We model the neutron star as perfect fluid, hence,

$$\tilde{T} = (\tilde{\rho}+\tilde{p})\tilde{u}^\mu\tilde{u}^\nu + \tilde{p}g^{\mu\nu}, \tag{3.5}$$

where $\tilde{u}$ is the four-velocity, $\tilde{p}$ is the pressure and $\tilde{\rho}$ is the energy density in the Jordan frame. which, in the end, is reduced to the following set of coupled ODEs

$$\begin{aligned}
\mu'(r) &= 4\pi r^2\mathcal{A}^4(\varphi)\tilde{\rho} + \frac{1}{2}r(r-2\mu)\psi^2,\\
\nu'(r) &= r\psi^2 + \frac{r^2}{r(r-2\mu)}\left[8\pi A^4(\phi)\tilde{p} + \frac{2\mu}{r^3}\right],\\
\varphi'(r) &= \psi,\\
\psi'(r)(r-2\mu) &= 4\pi r\mathcal{A}^4(\varphi)\left[\alpha(\varphi)(\tilde{\rho}-3\tilde{p}) + r\psi(\tilde{\rho}-\tilde{p})\right] - 2\psi(1-\mu/r),\\
\tilde{p}'(r) &= -(\tilde{\rho}+\tilde{p})\left(\nu'/2 + \alpha(\varphi)\psi\right),
\end{aligned} \tag{3.6}$$

where $()'$ denotes the derivative with respect to the radial coordinate. Very similarly for the sGB model, we have the field equations

$$R_{\mu\nu} - \frac{1}{2}Rg_{\mu\nu} + \Gamma_{\mu\nu} = 2\nabla_\mu\varphi\nabla_\nu\varphi - g_{\mu\nu}\nabla_\alpha\varphi\nabla^\alpha\varphi + 8\pi T_{\mu\nu}, \tag{3.7}$$

$$\Box\varphi = -\beta_{\mathrm{GB}}\frac{\mathrm{d}f(\varphi)}{\mathrm{d}\varphi}\mathcal{G}, \tag{3.8}$$

where $\Gamma_{\mu\nu}$ is defined by

$$\begin{aligned}\Gamma_{\mu\nu} \;\equiv\; & -R(\nabla_\mu\Psi_\nu + \nabla_\nu\Psi_\mu) - 4\nabla^\alpha\Psi_\alpha\left(R_{\mu\nu} - \frac{1}{2}Rg_{\mu\nu}\right) + 4R_{\mu\alpha}\nabla^\alpha\Psi_\nu \\ & +4R_{\nu\alpha}\nabla^\alpha\Psi_\mu - 4g_{\mu\nu}R^{\alpha\beta}\nabla_\alpha\Psi_\beta + 4R^\beta{}_{\mu\alpha\nu}\nabla^\alpha\Psi_\beta\,, \end{aligned} \tag{3.9}$$

with

$$\Psi_\mu \equiv \lambda^2\frac{\mathrm{d}f(\varphi)}{\mathrm{d}\varphi}\nabla_\mu\varphi. \tag{3.10}$$

Finally, one reaches the following modified TOV equations under the assumptions that the matter is perfect fluid and the system respects spherical symmetry and staticity

$$\begin{aligned}
&\frac{2}{r}(1+\frac{2}{r}(1-3e^{-2\Lambda})\Psi_r)\Lambda' + \frac{(e^{2\Lambda}-1)}{r^2} - \frac{4}{r^2}(1-e^{-2\Lambda})\Psi_r' - \varphi'' &&= 8\pi\rho e^{2\Lambda},\\
&\frac{2}{r}(1+\frac{2}{r}(1-3e^{-2\Lambda})\Psi_r)\Phi' - \frac{(e^{2\Lambda}-1)}{r^2} - \varphi'' &&= 8\pi p e^{2\Lambda},\\
&\Phi''+\Phi'+\frac{1}{r}(\Phi'-\Lambda') + \frac{4e^{-2\Lambda}}{r}\left[3\Phi'\Lambda' - \Phi'' - (\Phi')^2\right]\Psi_r &&\\
&\qquad -\frac{4e^{-2\Lambda}}{r}\Phi'\Psi_r' + (\varphi')^2 &&= 8\pi p e^{2\Lambda},\\
&-\frac{2\lambda^2}{r^2}\frac{df(\varphi)}{d\phi}\left\{(1-e^{-2\Lambda})\left[\Phi''+\Phi'\left(\Phi'-\Lambda'\right)\right] + 2e^{-2\Lambda}\Phi'\Lambda'\right\} &&\\
&\qquad \varphi'' + \left(\Phi' - \Lambda' + \frac{2}{r}\right)\varphi' &&= 0,
\end{aligned} \tag{3.11}$$

with again $()'$ denotes derivative w.r.t. the radial coordinate and

$$\Psi_r = \lambda^2\frac{\mathrm{d}f(\varphi)}{\mathrm{d}\varphi}\frac{\mathrm{d}\varphi}{\mathrm{d}r}. \tag{3.12}$$

3.2 Methods

The methodology that is followed in this chapter closely follows the one in [29] and can be summarized as follows: First, one must obtain every possible solution to the TOV equations, presented in the previous chapter to obtain a mass-radius curve (Sec. 3.2.1). Second, one must eliminate the unstable solutions and repeat this procedure by changing the parameters (β for DEF or $(\beta_{\rm GB}, \sigma)$ for sGB) of the model (Sec. 3.2.2). Finally, one must assign a likelihood to every mass-radius curve obtained, hence, every modified gravity theory, and constrain them if possible using Bayesian inference (Sec. 3.2.3).

3.2.1 Mass-Radius Curves

Obtaining the neutron star structure for a given model with parameters β or $(\beta_{\rm GB}, \sigma)$ is the first step of the analysis. To do this, one must numerically compute the modified TOV equation (3.6) and (3.11), which can be done by treating the problem as a boundary value problem and implementing a relaxation scheme [29, 40, 41]. Once an EOS is chosen, the set of TOV equations becomes a complete set and can be solved to give a neutron star solution. Then one can continuously change the boundary condition at the center of the star, namely the energy density at the core of the star, to find a set of neutron stars with different masses and radii. This set of neutron stars forms a continuous curve in the Mass-Radius plane. A straightforward example of such a curve in GR with different EOS can be seen in Fig. 3.1.

It is also essential the note that this process contains some uncertainties. The first of these uncertainties comes from our lack of understanding of nuclear matter inside the neutron stars, i.e., our limited understanding of the exact form of EOS. As can also be seen from Fig. 3.1, EOS also affects the Mass-Radius curves. In fact, the dataset we use was initially used to constrain the EOS. Therefore, we repeat our analysis for five different piecewise-polytropic EOS ranging from the softest (2B) to the stiffest (2H), which is sufficient for observing the effect of EOS in our analysis. We also marginalize over these EOS to minimize the effect of the EOS and see the effect of scalarization only.

Second, our simplifying assumptions while numerically solving the TOV equations, namely the spherically symmetric spacetime (3.4), increase the uncertainty in our calculations. This assumption is not valid in general due to the fact that neutron stars have spin. This is especially problematic if neutron stars rotate fast[1].

[1] to best of our knowledge, the spin of some of the neutron stars presented here is known, but for the rest, there isn't a known value

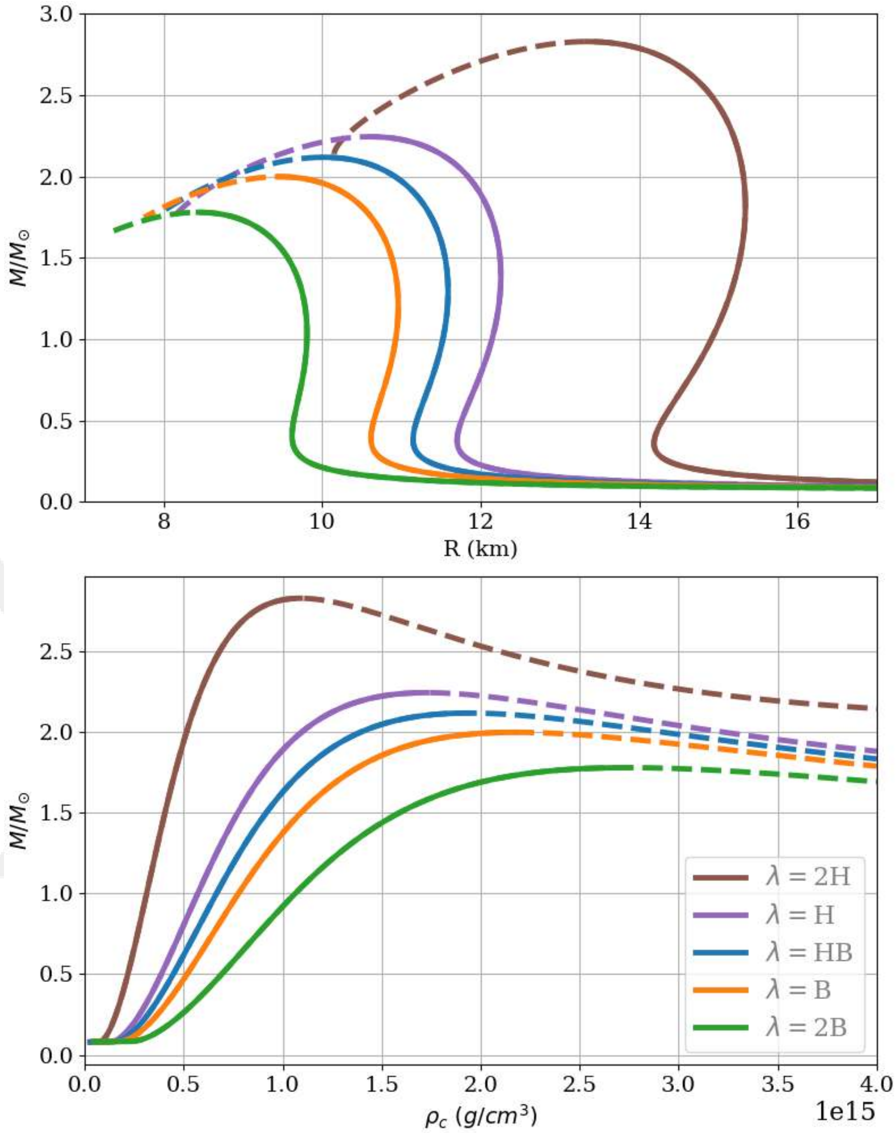

Figure 3.1: Mass-Radius curves in GR with different EOS used in this study. Dashed lines represent the hydrodynamically unstable solutions, while solid lines are stable. See 3.2.2 for more details on hydrodynamical stability.

Usually, in scalarization scenarios, the effect of rotation is negligible, though there are some extreme cases as well [42].

Finally, the mass-radius measurements of neutron stars used in the analysis are obtained under the assumption that GR is the theory of gravity. In GR, the definition of the mass of the star is more straightforward since outside the star; the metric is simply in Schwarzschild form with a single mass parameter. The situation is different in the case of scalarization, where the mass parameter of the metric becomes a function of radial distance r since the scalar field configuration around the star also contributes to the total mass and has a nonzero value outside the star as well. Therefore, in this study, we use Arnovit-Deser-Misner (ADM) mass as our mass parameter, which roughly measures the deviations of the metric from the flat metric. It has been shown in [40] that the choice of the mass parameters quantitatively changes the results, though the overall behavior does not change.

All these uncertainties mentioned above mean that, even if we find a higher than GR likelihood for a specific gravity model, we won't be able to make a precise conclusion. But this does not mean that a Bayesian analysis using mass-radius data is in vain, as it is possible to make a conclusion in the opposite direction and constrain certain gravity models. One example is the DEF model in Ref. [40] and extensions of the DEF model together with the sGB model in Ref. [29], which will be outlined here. The Bayesian analysis allows us to constrain certain gravity models because these theories deviate considerably from GR; therefore, some parts of the parameter space can be ruled out based on our mass-radius data.

3.2.2 *Stability of Solutions*

There is a balance in neutron stars between the gravitational pull inward and the pressure outwards due to the nuclear matter inside them. A neutron star is said to be stable if this balance is not broken when perturbed from its initial configuration. These are the astrophysically relevant neutron stars; therefore, we included only these stars in our analysis. There are two different criteria for a solution to the TOV equation to be stable. One is the hydrodynamic instability condition given as

$$\frac{\mathrm{d}M}{\mathrm{d}\tilde{\rho}_c} > 0. \tag{3.13}$$

where M is the mass of the star and $\tilde{\rho}_c$ is the central density of the star in the Jordan frame. In other words, if the condition (3.13) is not satisfied, we say the solution is *hydrodynamically unstable*.

An intuitive understanding of this condition is as follows: Assume the condition does not hold. That means that increasing central density, i.e., a more dense star, yields a star with less mass, therefore, less total energy. We expect a less energetic configuration to be preferred. But in this case, the less energetic configuration is also more dense, hence, has a smaller radius. Therefore, a smaller radius is always preferred, i.e., inward-directed perturbations are energetically favored, or simply put, the star collapses.

It is important to note that the condition (3.13) does not work both ways. In other words, while not satisfying the condition is enough to deduce hydrodynamical instability, fulfilling it is insufficient to conclude that the neutron star is hydrodynamically stable. One specific example is the DEF model for $\beta > 0$. Suppose one performs a quasinormal mode analysis of a scalarized neutron star that satisfies the condition (3.13) in this model. In that case, one can show that under small perturbations, modes grow exponentially. Hence, it is evident that these solutions are not astrophysically relevant [25]. Nevertheless, for the sake of completeness, we also provide an analysis for this model in Sec. 3.3.1.

There is also another type of instability that we should emphasize, which is scalarization. As we already explained in Sec. 2.1, the underlying mechanism for scalarization is due to tachyonic instability. That is, the scalar field can exponentially grow due to this instability; nevertheless, it can be quenched by the nonlinear effects later on. However, not every instability necessarily ends up in a stable configuration. For example, there are some cases where a neutron star solution in GR has tachyonic instability, i.e., wants to scalarize, but there is no corresponding scalarized solution with the same mass. So, what will happen if we start with such as star and try to evolve it? One possible answer is that the star may move to a less massive scalarized solution by losing some of its mass via radiation, either scalar or gravitational. Or another possibility is that the star collapses into a black hole. The ultimate answer requires a nonlinear evolution of the problem, though there aren't many studies on this matter in the literature [43].

It is possible to linearize the equations (3.1) and perform spherical mode analysis to investigate any star. This approach results in a schrödingerlike equation [20] and one can determine whether a solution has a tachyonic instability or not (see Sec. 2.1). Though, it is easier to determine via the neutron star mass since the scalarization depends on the mass of the star. For example, for the quadratic DEF model, the tachyonic instability exists only after some minimal mass value corresponding to a minimum central density. Though this does not necessarily mean that all the star above this mass also has tachyonic instability. This is because the trace of the stress-energy tensor can start to become less negative as the pressure becomes more important, $\tilde{T} = -\tilde{\rho} + 3\tilde{p}$. In other words, only a range of GR stars between some maximum and minimum mass can attain tachyonic instability, and the rest might be stable. However, the situation might be such that $\tilde{T}$ might never be small enough depending on the EOS and β, where all GR solutions above some mass value are scalarized. The situation is very similar for linear DEF as well.

The situation is a bit different for the $\beta > 0$ since we now require $\tilde{T} > 0$ for tachyonic instability. This typically happens for massive stars, and $\tilde{T}$ grows monotonically after that point. Therefore, there is no upper limit to the tachyonic instability. In other words, once we determine the least massive star which has a tachyonic instability, all the stars above will also have tachyonic instability. The $\mathscr{G}$ has a very similar role in the sGB model, and therefore, we can conclude that once we find a scalarized solution in the sGB model, all solutions with a higher mass also scalarize. However, we should restate that the ultimate answer lies in the nonlinear evolutions of these systems, and all the perturbative analysis performed so far approved our discussion [11, 20, 25].

M-R curves in DEF model

The mass-radius curves obtained for both the linear and the quadratic DEF models can be found in Fig. 3.2, where they have been plotted together for comparison. The first thing to notice from this figure is the amount of deviation from GR in each model. For each value of β, we see that the quadratic DEF always deviates more than the linear one. Therefore, without doing any analysis, we can predict that it will be hard to constrain the linear DEF model compared to the quadratic

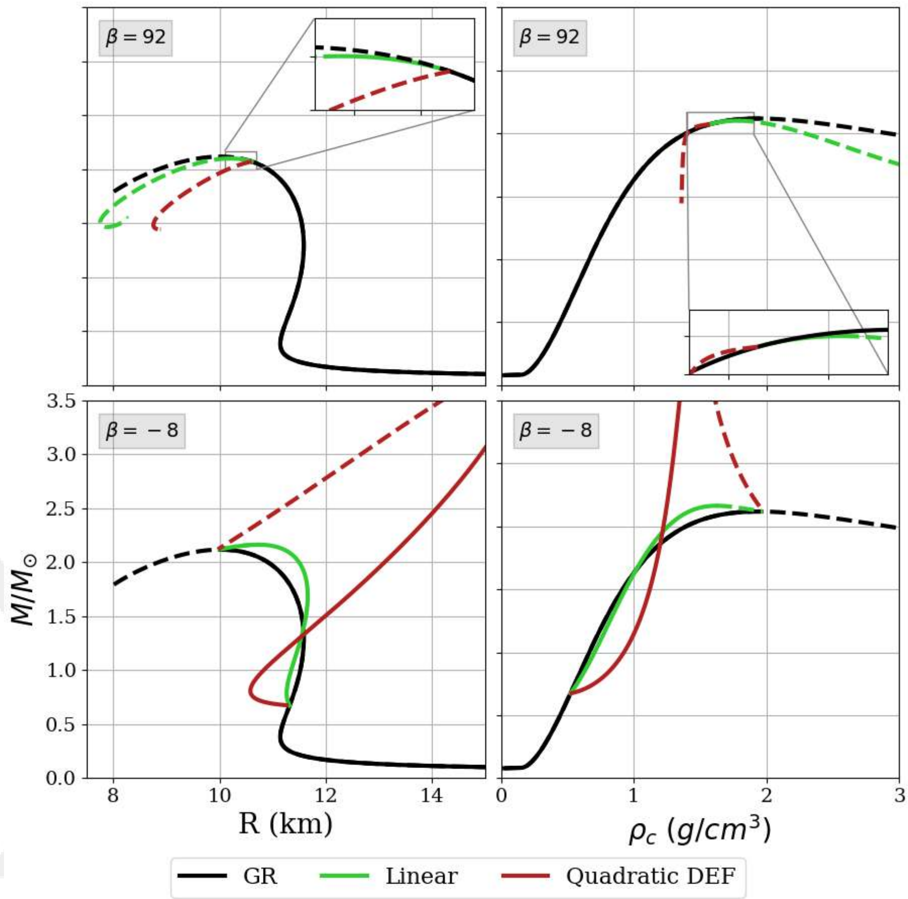

Figure 3.2: Mass-radius curves for Linear DEF model (green) and Quadratic DEF model (red), for $\beta = 92$ (top) and $\beta = -8$ (bottom). The right ones are mass vs. central density, and the left ones are mass vs. radius plots. λ = HB EOS used for each cases. Solid lines refer to astrophysically relevant stable solutions, whereas dashed lines are unstable ones.

since the former closely resembles GR.

Also, we need to have m_{eff} defined in Eq. (2.17) to be negative enough to have scalarization. Therefore, the value of $|\beta|$ should be great enough to ensure that. Furthermore, we expect the mass-radius curves to change continuously as we change the β; hence, it is expected that the smaller the value of β, the closer the theory to GR. And similarly, the greater the value of β, the greater the deviations from GR, as has been confirmed in the previous works [11].

It is also important to note that the maximum possible neutron star mass computed is always less than the one in GR for the $\beta > 0$, e.g., see Fig. 3.2 upper left panel. This is due to the fact that every star that is more massive than the most massive scalarized star has tachyonic instability. Therefore, any star after that point is astrophysically irrelevant.

M-R curves in sGB model

Mass-radius curves for different values of the parameters β_{GB} and σ are given in Fig. 3.3. As can be verified from the curves in the figure, the effect of the parameter β_{GB} in sGB, very similar to β in DEF, is to determine the onset of the scalarization, i.e., if there is tachyonic instability or not. Whereas the effect of σ is to determine the end state of this instability, in other words, to determine the final structure of the neutron star. Therefore, all the curves with the same value of β_{GB} branch from the GR curve at the same point but depending on the value of σ, they take different shapes.

Looking at the Eq. (2.23), we can conclude, similar to the DEF, that there are scalarized solutions only above a particular value of β_{GB}. Hence, the scalarization starts earlier for higher values, and for the lower values, it starts very late and approaches GR by not scalarizing at all. For the σ, however, the effect is similar to the effect of adding mass to the scalar field in the DEF model [27], that is, to suppress the scalarization as σ grows. In summary, as it is apparent in Fig. 3.3, the trend of the parameters is such that the theory approaches GR as $\beta_{\mathrm{GB}} \to \infty$ and $\sigma \to \infty$.

One last important aspect of the mass-radius curves in the sGB model is the fact that for every value of β_{GB}, there are some values of σ below some critical value $\sigma = \sigma_{\mathrm{crit}}(\beta_{\mathrm{GB}})$ such that all the scalarized solutions do not satisfy the condition (3.13). In other words, we have

$$\sigma < \sigma_{\mathrm{crit}}(\beta_{\mathrm{GB}}) \implies \text{no scalarized stable solutions} \tag{3.14}$$

These curves branch out from GR with a negative slope in the second plot in Fig. 3.3 and will not be considered in our analysis as they are not astrophysical solutions.

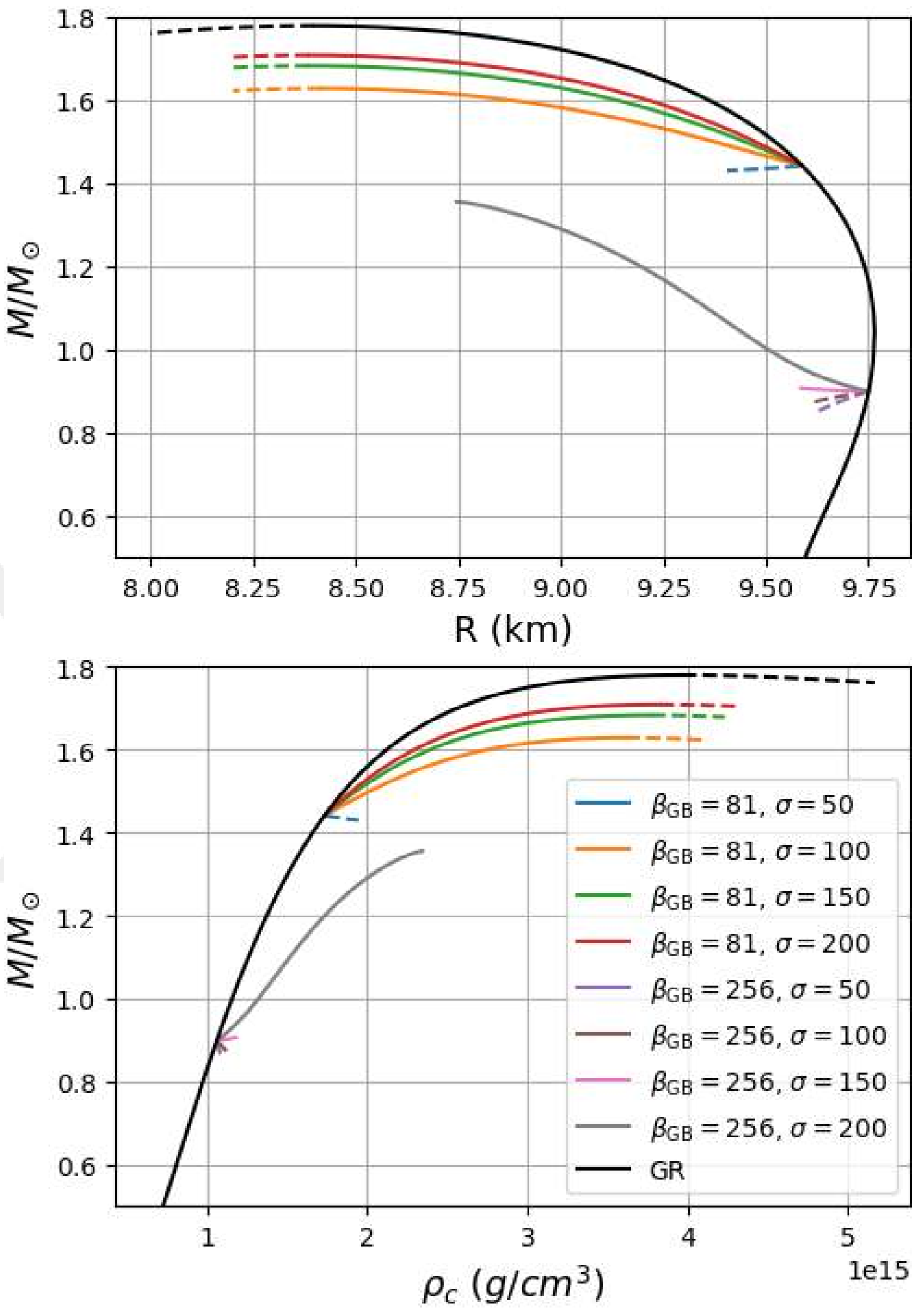

Figure 3.3: Mass-radius (top) and mass-central density (bottom) curves for the sGB model for various values for the parameters β_{GB} and σ. Similar to Fig. 3.2, the dashed lines represent the hydrodynamically unstable solutions, whereas the solid lines represent the stable ones. 2B EOS is used for all curves.

3.2.3 Bayesian Analysis

In this section, we briefly lay out the details of the analysis that is performed in this study, which closely follows the ones in [29, 39, 40]. After obtaining the mass-radius curves by numerically computing TOV equations as described in Sec. 3.2.1 and eliminating the unstable solutions as described in Sec. 3.2.2 for different sets of dimensionless parameters $\{\pi\}$ for each model, namely (β, λ) for DEF and $(\beta_{\rm GB}, \sigma, \lambda)$ for sGB where λ stands for EOS, we assign likelihood to each curve by making use of the Bayes' Theorem given as

$$P(\{\pi\}|\text{data}) = \mathcal{N} P(\text{data}|\{\pi\}) \mathrm{P}_{\rm Pri}(\{\pi\}) \,, \tag{3.15}$$

where $\mathcal{N}$ is just a normalization constant. The dataset used in this study is slightly larger than the one in Ref. [40]. In particular, we have the mass-radius measurements of 12 neutron stars from Ref. [39], two from Ref. [44], and lastly, two new measurements from the Refs. [45–48][2]. But these measurements are not precise, i.e., each of these measurements gives a likelihood distribution, $P_i(M, R)$, where i is the index for each star. Therefore, to calculate the second term in Eq. (3.15), we can write it as the product of each likelihood distribution as

$$P(\text{data}|\{\pi\}) = \prod_{i=1}^{N=16} P_i(M, R|\{\pi\}) \,. \tag{3.16}$$

Typically, there is a unique neutron star for a given total mass M[3]. Hence, we can think of each mass-radius curve as a one-to-one function of mass for a given set of parameters $\{\pi\}$, $R = R(M; \{\pi\})$. Then we can turn each term in Eq. (3.16) to an

[2]The new stars, namely J0030+0451 [45, 46] and PSR J0740+6620 [47, 48] were studied by two research groups. Therefore, we gave half weight to each reported mass-radius measurement. There are also other measurements reported by other groups [49–52]. However, due to the absence of a likelihood distribution of stellar mass and radius, we could not include these stars in our analysis

[3]There are cases where there are two stars for a given mass with different radii. However, it is always the case that one of these solutions is hydrodynamically unstable, therefore, does not contribute to our analysis.

integral over M as

$$P_i(M,R|\{\pi\}) = \mathcal{N}_2 \int_{M_{min}}^{M_{max}} P_i(M,R(M;\{\pi\}) \times \mathrm{P}_{\mathrm{Pri}}(M)\,\mathrm{d}M. \tag{3.17}$$

In other words, the above integral over the mass-radius curve gives the likelihood of the data, indexed i, for a given set of parameters. Then, one can multiply these to obtain the overall likelihood of the whole data set, which later can be used in Eq. (3.15) to calculate the likelihood of the given set of parameters $\{\pi\}$. Of course, to achieve this, one must define a prior for the parameters, $\mathrm{P}_{\mathrm{Pri}}(\{\pi\})$, which brings us to the next section.

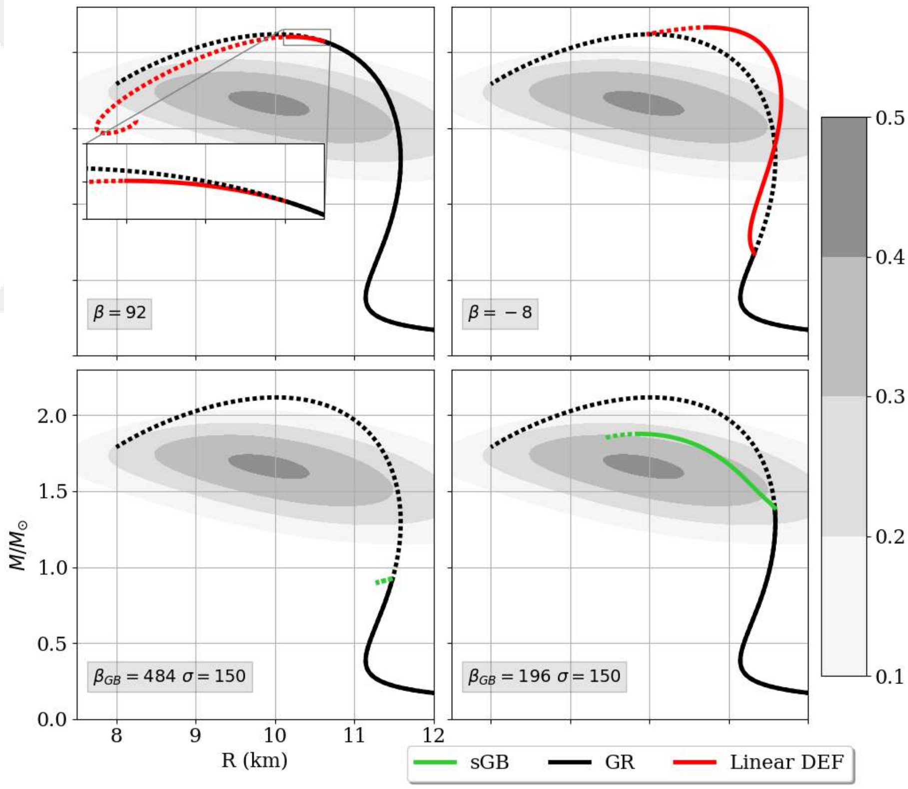

Figure 3.4: Mass-radius curves for Linear DEF (red) and sGB (green) models on top of the probability distribution of an NS KS1731-260 as a contour plot in greyscale. Dashed lines represent the unstable stars which do not play a role in our analysis, and the solid ones are the stable ones.

Priors

We will be using two different priors for the Bayesian analysis. The first one, which we will refer to as *simple flat prior*, is the flat distribution over a finite range for all parameters: for the quadratic DEF $\beta \in [-100, 160]$; for the linear DEF $\beta \in [-202, 212]$; for the sGB model $\beta_{\mathrm{GB}} \in [36, 900]$, $\sigma \in [50, 700]$. This is the most trivial choice for this kind of analysis as there is no preferred range apart from the fact that they are expected to be the order of unity since they all are dimensionless quantities. However, for the sGB model, there are some subtleties that we must point out. First, it has been known that the theory has some well-posedness problems for the high values of β_{GB}, which are purely theoretical [53–55]. Therefore, an upper bound for this parameter is highly motivated, and $\beta_{\mathrm{GB}} = 0$ is already identical to GR. For the σ, however, it is quite the opposite, i.e., in the limit $\sigma \to \infty$, the model gives identical results. This implies that there is an infinitely large region in the parameter space for σ, which is identical to GR but with a more complex theory. We want to eliminate this region; hence, we put a cutoff at 700, which is a reasonable choice since we expect these parameters to be the order of unity, as mentioned earlier.

The second prior we consider in this study is again a flat distribution, but this time we make some restrictions based on other observations, namely, the observation of a neutron star whose mass is around $2.35 \pm 0.17 M_{\odot}$. Therefore, this measurement rules out any model that does not meet the requirement of having a maximum neutron star mass of at least this value. Though, there are some other factors, such as high spin, that can increase the maximum possible mass in a given model. Hence, we picked a value of at least $2M_{\odot}$ for the maximum neutron star mass, and restricted our attention to those models that meet this requirement, i.e., we excluded every model which does not have a massive enough star that has $2M_{\odot}$. We call this prior *restricted prior*.

Restricted prior already rules out the 2B and B EOS for GR, but the high mass a neutron star can attain increases in the scalarization scenario. Therefore, we included these EOS in our analysis as well; however, in the end, as we will see, it turns out the picture stays the same, and these EOS are ruled out nevertheless.

We should also mention that there are some bounds to these parameters coming from binary observations [56] as well as some cosmological considerations [57]. Though, these constraints are not valid once a mass term is introduced in the Action. Therefore, even the large values such as $|\beta| = 200$ and $\beta_{\mathrm{GB}} = 900$ are of our interest. In addition, we know that the theory continuously changes with the mass parameter m_φ and becomes identical to GR when $m_\varphi = 0$. Hence, even though we analyzed the massless scalar theory, our results also give information about the $m_\varphi \neq 0$ case where the mass is small.

In short, both priors use the flat distribution over the same range; however, while the analysis with the simple flat prior solely relies on mass-radius measurements from x-ray data, the restricted prior also uses other observations. Apart from the fact that the restricted prior rules out 2 of the EOS we use, two priors we use give qualitatively similar results, as we shall see in the next section.

3.3 Results

In this section, we will present the results of the Bayesian analysis of the previous part. The relevant results are taken from Ref. [40] for the quadratic DEF with $\beta < 0$ and from Ref. [29] for the rest.

3.3.1 Linear DEF model

After applying the Bayesian analysis to the DEF model, one ends up with the posterior distribution of the model calculated from Eq. (3.15) with the dimensionless parameter β and EOS λ. Then we can define a conditional posterior probability as

$$P^{\lambda}_{\mathrm{cond}}(\beta) \equiv \mathcal{N} P(\beta, \lambda|\mathrm{data}) \,, \tag{3.18}$$

We then define the marginal probability by marginalizing over λ as

$$P_{\mathrm{marg}}(\beta) \equiv \sum_{\lambda} P(\beta, \lambda|\mathrm{data}) = \sum_{\lambda} P^{\lambda}_{\mathrm{cond}}(\beta). \tag{3.19}$$

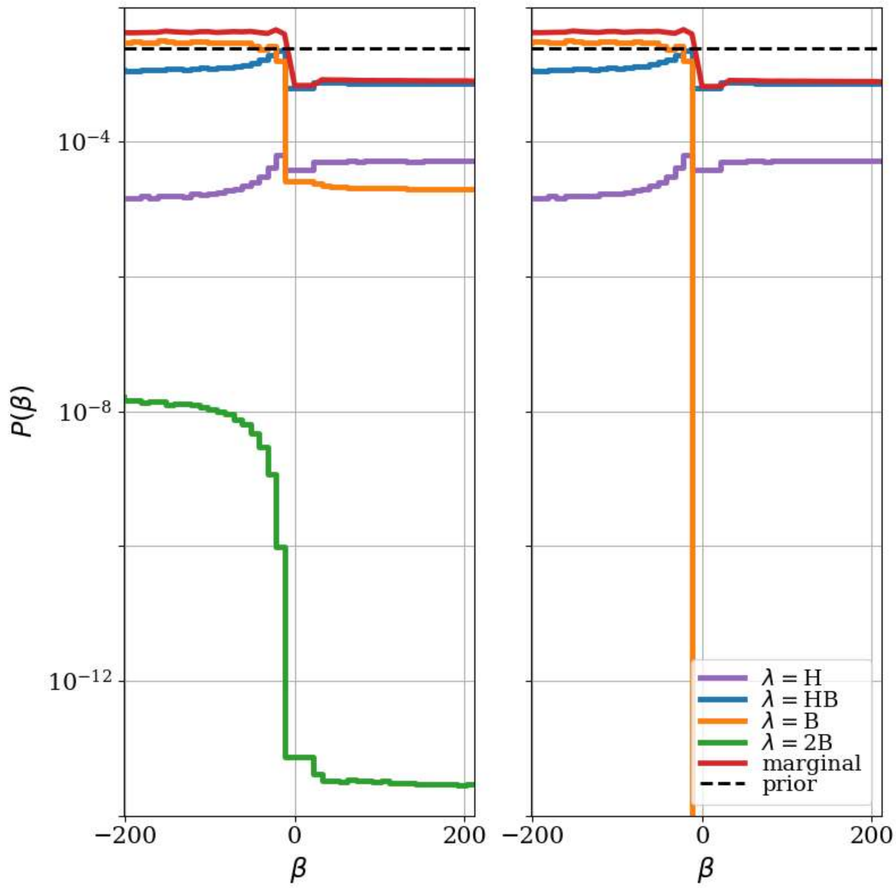

Figure 3.5: Conditional probability distribution, $P^{\lambda}_{\rm cond}(\beta)$, and marginalized probability distribution $P_{\rm marg}(\beta)$ of the parameter β in the linear DEF model. 2B EOS is not present since it does give either vanishing or negligible contribution to the posterior.

The Eq. (3.18) is useful to see how the posterior distribution changes with each EOS, i.e., how much our results depend on our understanding of nuclear physics. It basically tells us the probability of the parameter β once an EOS is chosen. Therefore, one can as well compare the EOS by looking at the relative probabilities. On the other hand, Eq. (3.19) gives the posterior distribution non-withstanding to the EOS. Both the distributions in Eq (3.18) and in Eq (3.19) for both of the priors mentioned in Sec. 3.2.3 are given in Fig. 3.5.

To begin with, we can infer some information from Fig. 3.5. For instance, for both *flat prior*, we see that the negative values of β are generally preferred over the positive ones. This trend is more clear for the 2B and B EOS and becomes less prominent for the HB EOS. Furthermore, we see that if we assume H EOS, there exists an inclination towards positive values. Nonetheless, the marginalized probability distribution averaged over all EOS does not provide sufficient information to conclude something useful as it is not very different from the prior. The situation is very similar for restricted prior, where the only difference is that positive values are entirely ruled out for B EOS, and we see no contributions from 2B EOS.

The main feature of Fig. 3.5 is that there is no decay as $|\beta| \to \infty$ for both priors, contrary to the case in the quadratic DEF model. Therefore, there might still be a nonzero probability for arbitrarily large values of $|\beta|$. This is due to the fact that the deviation from GR in mass-radius curves approaches some value as we move further in the parameter space. Furthermore, deviations itself is not much compared to the quadratic case. Hence, these two main aspects of the mass-radius curves in this model prevent us from having a decaying posterior distribution, and therefore, we are unable to constrain the model. This is the first result of this study.

It is also important to point out that the usual understanding of scalarization as the large deviations from GR in the strong field regime is not necessarily true. This has been confirmed, as we showed in this section. Just changing the coupling function of the theory, i.e., changing from quadratic DEF to linear DEF, gives a theory that deviates much less from GR.

3.3.2 sGB model

Our analysis of the scalar-Gauss-Bonnet model is very similar to the one for the DEF model presented in the previous section. The only difference is the fact that we now have two dimensionless parameters, $(\beta_{\mathrm{GB}}, \sigma)$, along with the parameter for EOS, λ. Therefore, we make similar definitions for prior distributions, which are 2-dimensional distributions over the $(\beta_{\mathrm{GB}}, \sigma)$ plane.

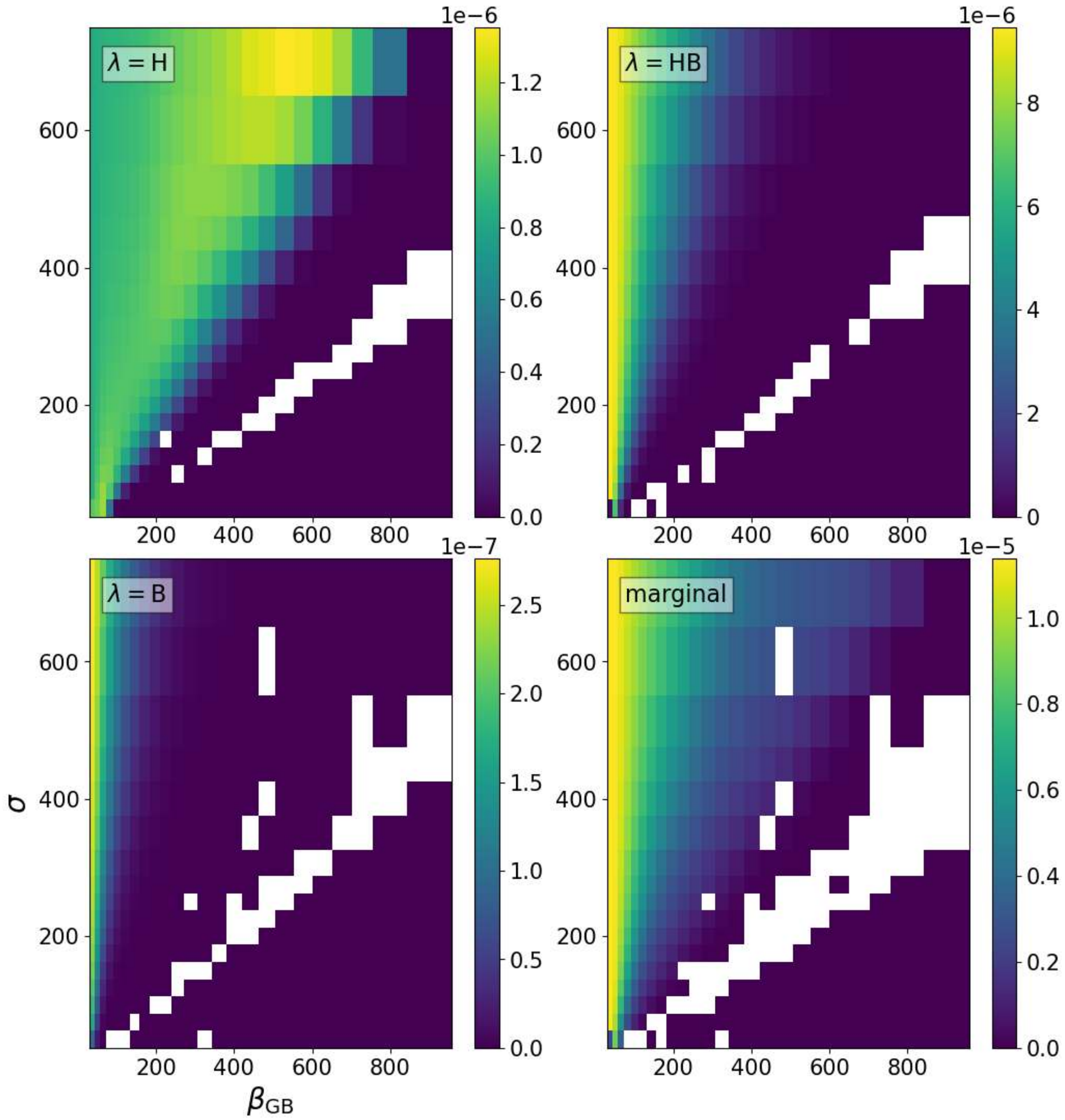

Figure 3.6: Conditional probability distribution over 2-dimensional parameter space $(\beta_{\rm GB}, \sigma)$, $P^{\lambda}_{\rm cond}(\beta_{\rm GB}, \sigma)$ for H, HB and B EOS, and marginalized posterior distribution, $P_{\rm marg}(\beta_{\rm GB}, \sigma)$ (lower right), for the sGB model. Other EOS have either a vanishing posterior or their contribution is negligible. White spots are the points where our numerical scheme failed near the region where the scalarized branches switch to unstable ones, i.e., around $\sigma_{\rm crit}(\beta_{\rm GB})$.

$$
\begin{aligned}
P^{\lambda}_{\rm cond}(\beta_{\rm GB}, \sigma) &\equiv P(\beta_{\rm GB}, \sigma, \lambda|{\rm data}) \, , \\
P_{\rm marg}(\beta_{\rm GB}, \sigma) &\equiv \sum_{\lambda} P(\beta_{\rm GB}, \sigma, \lambda|{\rm data}) \, ,
\end{aligned}
\tag{3.20}
$$

where $P^{\lambda}_{\text{cond}}(\beta_{\text{GB}},\sigma)$ is the conditional prior distribution and $P_{\text{marg}}(\beta_{\text{GB}},\sigma)$ is the marginalized prior distribiıtion which is averaged over all EOS. Furthermore, we define 1-dimensional probability distributions for each parameter by marginalizing over the other to be able to see how the distribiıtions of individual parameters change

$$\begin{aligned}
P^{\lambda}{}_{\text{cond}}(\beta_{\text{GB}}) &\equiv \int_0^{\infty} P^{\lambda}_{\text{cond}}(\beta_{\text{GB}},\sigma)\,\mathrm{d}\sigma\,, \\
P_{\text{marg}}(\beta_{\text{GB}}) &\equiv \int_0^{\infty} P_{\text{marg}}(\beta_{\text{GB}},\sigma)\,\mathrm{d}\sigma\,, \\
P^{\lambda}{}_{\text{cond}}(\sigma) &\equiv \int_0^{\infty} P^{\lambda}_{\text{cond}}(\beta_{\text{GB}},\sigma)\,\mathrm{d}\beta_{\text{GB}}\,, \\
P_{\text{marg}}(\sigma) &\equiv \int_0^{\infty} P_{\text{marg}}(\beta_{\text{GB}},\sigma)\;\mathrm{d}\beta_{\text{GB}}\,.
\end{aligned} \tag{3.21}$$

The posterior distributions in Eq. (3.20) can be seen in Fig. 3.6 for H, HB, and B together with the marginalized distribution. There were some expected trends, as explained in Sec. 3.2.1, that can be verified in these plots. For instance, we expect the theory to converge to GR in the sense that the solutions one obtains are identical to those in GR. As a result, we see that the likelihood is the same around the region $\beta_{\text{GB}} \to 0$, which is the likelihood of GR. Another trend we can see is the existence of a curve, $\sigma_{\text{crit}}(\beta_{\text{GB}})$, where all the scalarized solution starts to become unstable under it; hence, all the theories below this curve is strictly less probable as they are simply a subset of their GR counterparts (see Fig.3.4). This region also has a small likelihood due to the reason that the curves barely overlap with the data. Also, note that the gaps in these plots around this region are due to the computational failures around this region.

Another aspect of Fig.3.6 is the differences in the distributions for each EOS, namely the qualitative difference between H, HB EOS, and B EOS. We did not include the 2H and 2B EOS as their contribution was negligible due to barely overlapping with the data. 2B EOS already had a very small likelihood in GR for predicting less maximum theoretical neutron star mass. In sGB, this amount is even less in every case (see Fig. 3.3). Furthermore, 2H EOS had little to no overlap with some of the data in the Linear model as well (see Fig. 3.5). The same holds true here; hence, zero likelihood for 2H EOS is calculated.

In Fig. 3.6, H and HB EOS clearly favor higher $\beta_{\rm GB}$ and σ values; however, the overall trend is dominated by B EOS, which does not share the same features as others. This is an important result one must keep in mind while obtaining the constraints that will be presented next.

To understand how one can constrain the model using the Bayesian Analysis (see Sec. 3.2.3), we can focus on Fig.3.7 where we plotted the conditional distributions for each parameter. In these plots, marginalized posterior distributions, $P_{\rm marg}(\beta_{\rm GB})$ and $P_{\rm marg}(\sigma)$ decays in an exponential or faster than exponential manner for the high $\beta_{\rm GB}$ and low σ values. This makes us able to constrain these parameters. Hence, for the flat prior, we get the following bounds at 95% confidence,

$$\begin{aligned} \beta_{\rm GB} &< 491\ , \\ \sigma &> 162\ . \end{aligned} \tag{3.22}$$

Additionally, we examined the sensitivity of these limits to the EOS by considering each EOS separately and repeating the analysis. The results for each EOS can be found in Table. 3.1.

EOS	95% bounds	
H	$\sigma > 175$	$\beta_{\rm GB} < 635$
HB	$\sigma > 158$	$\beta_{\rm GB} < 318$
B	$\sigma > 176$	$\beta_{\rm GB} < 187$
2B	$\sigma > 308$	$\beta_{\rm GB} < 67$

Table 3.1: bounds for the theory parameters for each EOS. The trend for σ is not apparent though for $\beta_{\rm GB}$ softer EOS allows us to constrain easily.

These bounds are in accordance with our expectations; see Sec. 3.2.1. Remember that the mass-radius curves diverge from GR as $\beta_{\rm GB} \to \infty$, and the theoretical maximum mass for a neutron star gets smaller as $\sigma \to 0$ making the curves and

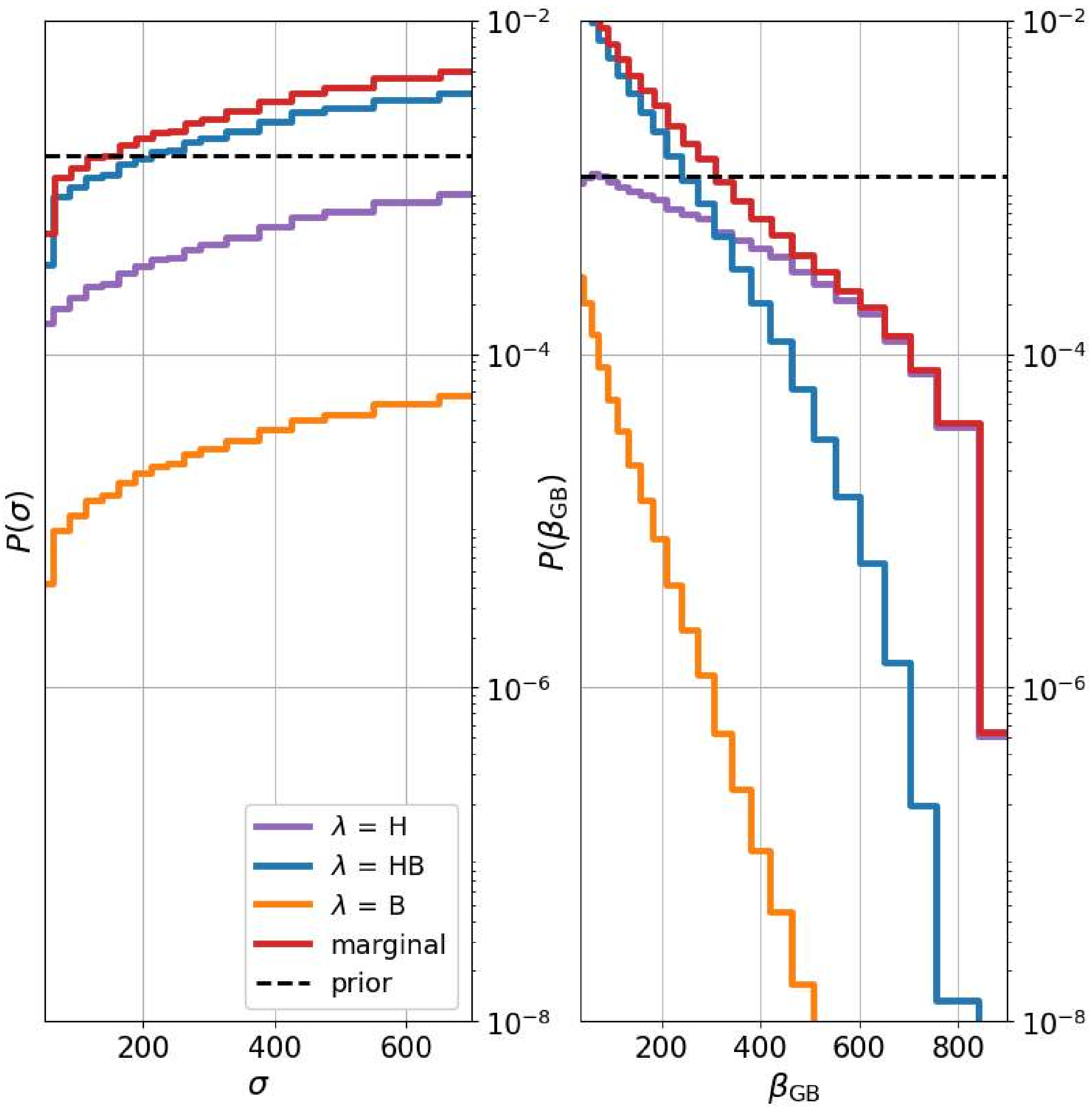

Figure 3.7: Conditional probability distribution over each parameter ${P^{\lambda}}_{\text{cond}}(\beta_{\text{GB}})$ and ${P^{\lambda}}_{\text{cond}}(\sigma)$, and their marginalized over each EOS counterparts, $P_{\text{marg}}(\beta_{\text{GB}})$ and $P_{\text{marg}}(\sigma)$ (red), using simple flat prior. 2H has a vanishing posterior, and 2B EOS behaves qualitatively similarly, but the values are too low to show in the figure. The decays $\beta_{\text{GB}} \to \infty$ and $\sigma \to 0$ results in the bound given in Eq. (3.22)

the data overlap less. In light of these observations, it makes sense to have an upper bound for β_{GB} and a lower bound for σ as in Eq. (3.22). However, there are also grounds for exercising caution about these results.

First, notice the dependence of qualitative behavior of $\beta_{\rm GB}$ to EOS in Fig. 3.7 and even more clearly in Table. 3.1. The likelihood decays exponentially as $\beta_{\rm GB} \to \infty$; however, the extent of this trend is milder for stiffer EOS and less prominently manifests itself in the case of H EOS. While the prevailing pattern is advantageous for achieving a constraint, it is worth noting the qualitative distinction among EOS. The bounds for σ change based on the EOS, yet a discernible pattern is lacking. Furthermore, three dominant EOS, namely H, HB, and B EOS, give a very similar result.

Finally, we repeat the same analysis with the restricted prior defined in Sec. 3.2.1, which can be seen in Fig.3.8. This yields the following constraints

$$\begin{aligned} \beta_{\rm GB} &< 427 \, , \\ \sigma &> 133 \, . \end{aligned} \tag{3.23}$$

at 95% confidence. These constraints are similar to the ones obtained before, given in Eq. 3.22, but they are more strict. Also, we see that 2B and B EOS are completely ruled out while the remaining ones decay faster or completely vanish after some point.

We should also emphasize the fact that there are other choices for dimensionless parameters in the literature. Namely, $\sqrt{\beta_{\rm GB}}$ is used in Doneva and Yazadjiev [20]. Our results are generic in the sense that they can provide bounds on any functions of σ and $\beta_{\rm GB}$. However, the exact bound may be subject to change since the choice of prior would be affected by our definition of the parameters. For example, in the case of $\sqrt{\beta_{\rm GB}}$, flat prior in our analysis is equivalent to a weighted distribiition. In this case, we would have a more stringent constraint, though other definitions might affect it in other ways.

In general, we find the constraint on $\beta_{\rm GB}$ to be somewhat less definitive compared to the constraint on β in the quadratic DEF model derived in Tuna et al. [40]. It is clear that there is an upper bound around some hundreds, though the exact value is not precise. Hence, given the bounds obtained in Eqs. (3.22) and (3.23), it would be more appropriate to report a bound of $\beta_{\rm GB} \lesssim 500$. There are some other constraints, potentially stronger than this one, coming from the hyperbolicity

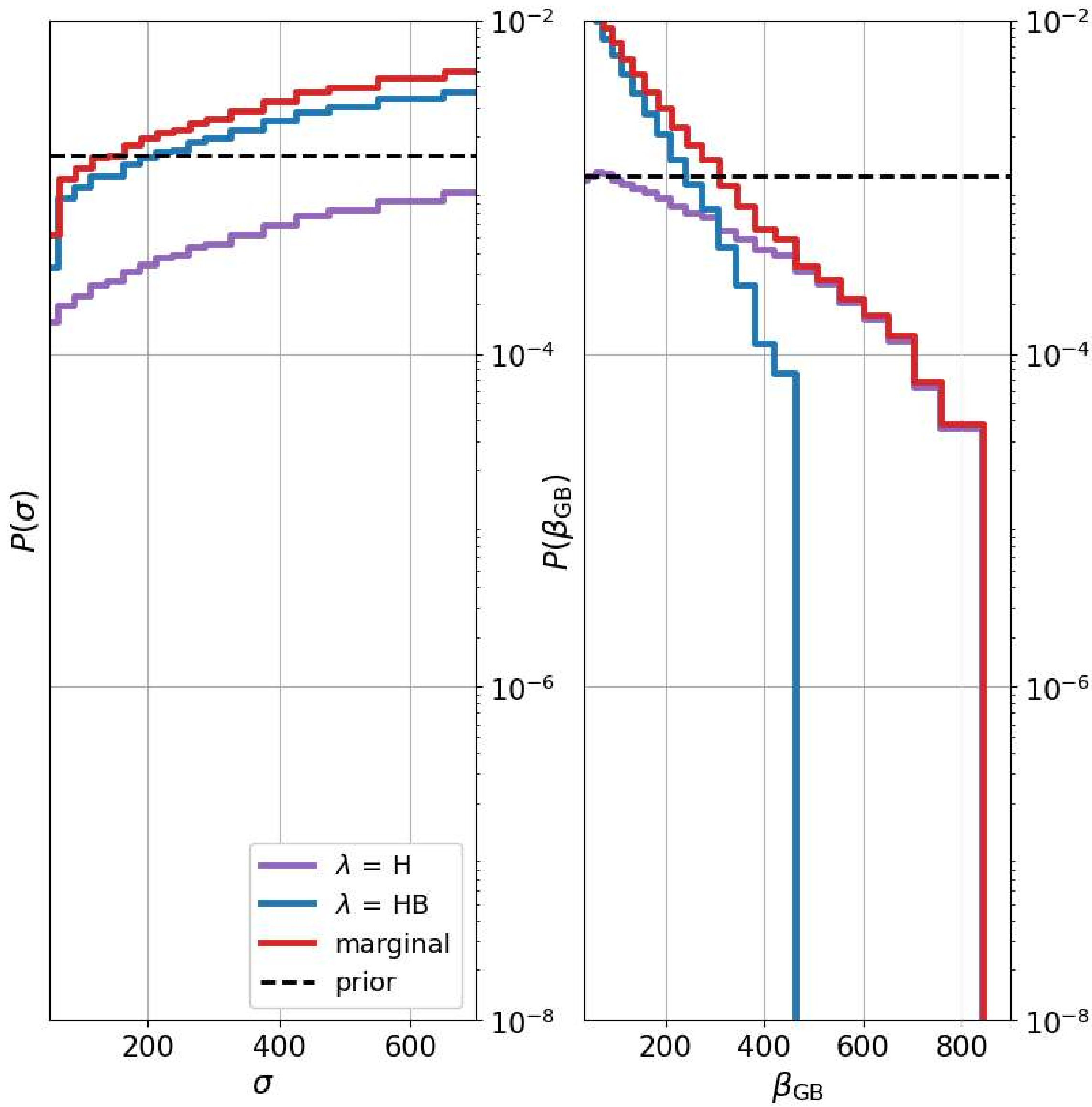

Figure 3.8: Same as Fig. 3.7 but for restricted prior. 2B and B EOS have zero likelihood due to not satisfying the condition of allowing a maximum neutron star mass of 2 $M_{\odot}$. 2H EOS was already giving no contribution; hence, only H and HB EOS remain with a nonzero likelihood.

considerations. But the interpretation of these is still under discussion [53–55]. On the other hand, the parameter σ already has a mechanism that does not allow it to be high, as we discussed. Furthermore, there might be the order of unity errors in our calculations due to the methodology, but we predict a soft bound of $\sigma \gtrsim 100$.

3.3.3 Effect of the dataset

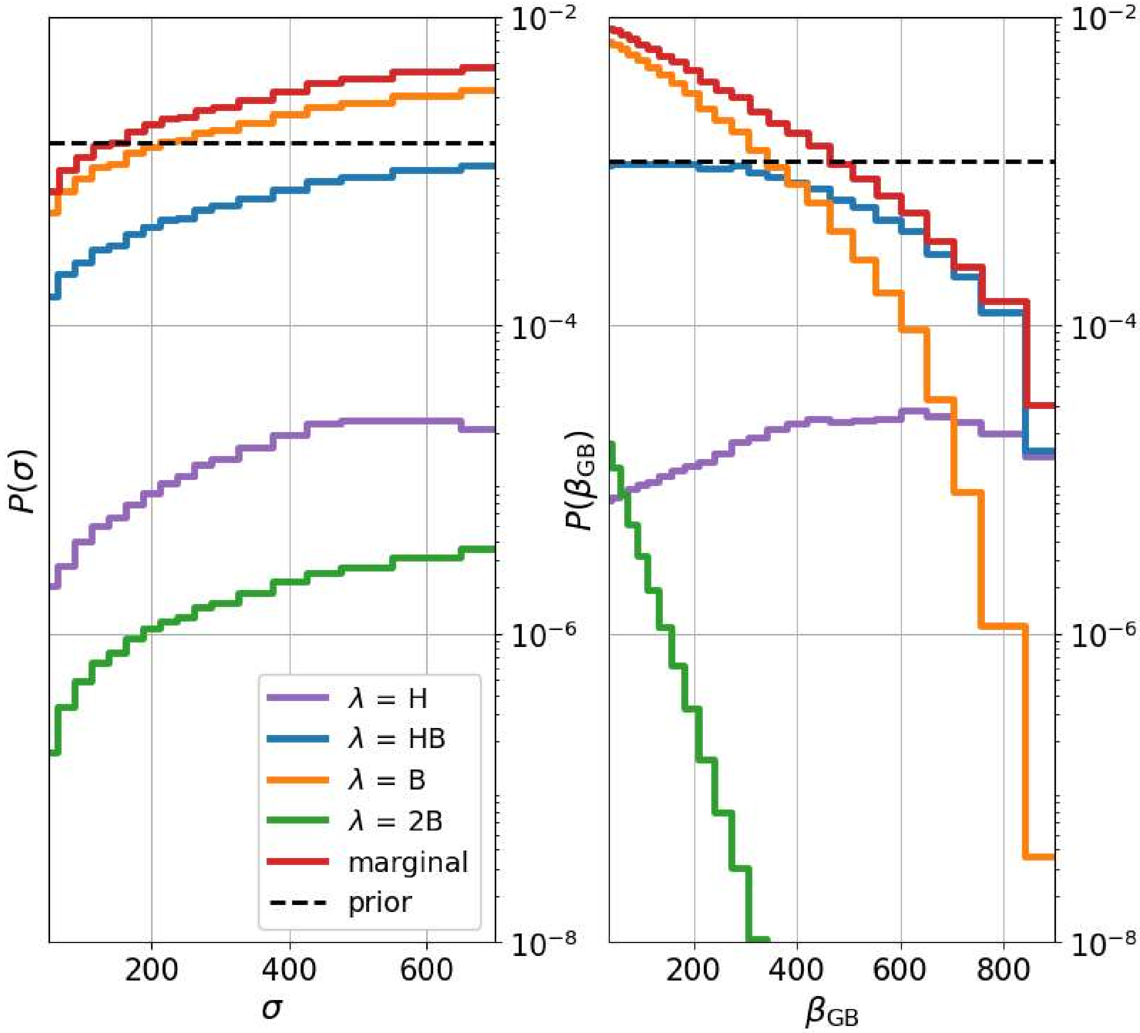

Figure 3.9: Same as Fig. 3.8 but for a smaller dataset where two newly added stars PSR J0030+0451 and PSR J0740+6620 are excluded. H EOS drastically differs since there is barely an exponential decay in this one, whereas in Fig. 3.8, it is much more evident.

The size of the dataset we used, namely the number of stars whose mass-radius measured, also affects the overall results. We included two more stars to our data set, which are PSR J0030+0451 [45, 46] and PSR J0740+6620 [47, 48] which were absent in the previous study [40]. Here we demonstrate the effect of adding these measurements by repeating our analysis without the newly added stars. The results for this analysis can be found in Table. 3.2 and Fig. 3.9. The bound we obtain by marginalizing over all EOS with a 95% confidence becomes

$$\begin{aligned} \beta_{\mathrm{GB}} &< 606\,, \\ \sigma &> 168\,. \end{aligned} \tag{3.24}$$

EOS	95% bounds	
H	$\sigma > 217$	$\beta_{\mathrm{GB}} < 859$
HB	$\sigma > 180$	$\beta_{\mathrm{GB}} < 697$
B	$\sigma > 162$	$\beta_{\mathrm{GB}} < 465$
2B	$\sigma > 191$	$\beta_{\mathrm{GB}} < 166$

Table 3.2: Same as Table. 3.1 but for a smaller dataset where two newly added stars PSR J0030+0451 and PSR J0740+6620 are excluded. Similar to the previous one, there is no clear trend on σ. However, for β_{GB}, all the bounds obtained are weaker compared to Table. 3.1. The bound for H EOS is very close to the maximum possible value we choose for our prior. Hence, it can be debatable the correctness of these values.

There are two major differences between these two analyses that we should point out. First, see the behavior of H EOS in Fig. 3.9 compared to the one in Fig. 3.7. The latter clearly shows an exponential decay similar to the other EOS, while the decay barely starts in our prior range for the former. In other words, the bound given in Eq.(3.24) is influenced by the cutoff in the prior, which was $\sigma = 700$. This means that changing the maximum value of σ in our prior might lead to different results. Therefore, the fact that there exists a bound for this EOS is debatable if we use the smaller dataset. However, with the addition of two more stars, we can clearly put bounds on the theory given in (3.22).

Second, the bounds obtained with the smaller dataset in Table. 3.2 are weaker compared to ones obtained with the larger dataset given in Table. 3.1. Although this is expected, the effect of a small decrease in the number of stars from 14 to

16 is noteworthy. This indicates that as we gather more data, this methodology can be successful in obtaining even more strict bounds on the theory. On the other hand, the same procedure applied to the linear DEF model yields no difference; that is, there are still no bounds obtained.

In summary, expanding observational efforts in the field of neutron star mass-radius measurements is significantly important, as was shown in this section.

Chapter 4

THEORETICAL TESTS OF SCALARIZATION

The most simple generalization to the scalarization is to extend the idea to vectors, namely vectorization [17, 18]. The main idea was to have a model where the vector field exhibits a linear tachyonic instability similar to scalarization. However, the existence of a third degree of freedom, with its dynamics being unclear, raises concerns about the effectiveness of this design(see Refs. [33, 34, 58–63]). We have already theoretically analyzed the growth of the scalar field by performing a perturbative analysis and showed the existence of tachyonic instabilities. Similarly, in this chapter, we will take one step further and will investigate the idea of vectorization in light of theoretical considerations. In particular, we will introduce the types of instabilities one faces in field theories (Section 4.1). Later, we will investigate a basic vectorization model analogous to the DEF model and see that the theory suffers not only from tachyonic instabilities as one would expect but from other pathologies as well (Section 4.3). Furthermore, by numerically computing all vectorized solutions, we will show that all spherically symmetric vectorized solutions suffer from these pathologies (Section 4.4).

4.1 Types of instabilities

We already defined what a tachyonic instability is in Sec. 2.1. Now, in this chapter, to have a complete picture, we will categorize the instabilities into three groups: tachyonic, gradient, and ghost. To this end, let us start from a basic 1+1 dimensional massive scalar field model on a fixed static background with the metric g. The Lagrangian is given by

$$S = \int \mathrm{d}x\,\mathrm{d}t\sqrt{-g}\Big[-\frac{1}{2}g^{\mu\nu}\partial_\mu\varphi\partial_\nu\varphi - \frac{1}{2}m^2\varphi^2\Big]. \tag{4.1}$$

The equation of motion follows from this action is

$$\Box\varphi = m^2\varphi^2 , \tag{4.2}$$

or in an open form, one can write it as

$$g^{tt}\partial_t^2\varphi + g^{xx}\partial_x^2\varphi = m^2\varphi^2 . \tag{4.3}$$

Note that for the sake of simplicity, we choose a static metric; hence, no cross terms. The solution to this equation can be decomposed into Fourier modes, $\varphi(t,x) = e^{-i[kx-\omega t]}$, with the following dispersion relation

$$\omega = \sqrt{\frac{m^2 + g^{xx}k^2}{-g^{tt}}} \tag{4.4}$$

Usually, we have $g^{tt} < 0$, $g^{xx} > 0$[1] and $m^2 > 0$ which results in real ω values. Therefore, Fourier modes oscillate in time with frequency ω as expected. However, if one gets imaginary values of ω, one gets exponentially decaying and growing modes, which is an instability.

First, let us consider the case where $m^2 < 0$. Then the modes that satisfy the condition

$$k^2 < \frac{-m^2}{g^{xx}} \tag{4.5}$$

are unstable. Hence it is an infrared instability. Note that there is an upper limit to the growth rate as the fastest growing mode will behave like $\sim e^{\sqrt{m^2/g^{tt}}t}$. This type of instability is called "tachyonic" instability. This is the type of instability that is responsible for the *scalarization* (See Sec. 2.1).

Second, consider the case where $g^{xx} < 0$. Similar to tachyonic instability, we have modes with wave numbers satisfying

$$k^2 > \frac{m^2}{-g^{xx}} \tag{4.6}$$

[1]Depending on the choice of metric signature, one gets the opposite. Here we adopt $(-,+)$ signature

unstable, and smaller ones stable. But this time, there is no limit to the growth rate as high wave number modes behave as $\sim e^{\sqrt{g^{xx}/g^{tt}}kt}$. This type of instability is called "gradient" instability.

Finally, consider the case where $g^{tt} > 0$. This means that the metric signature became $(+,+)$; hence there is no concept of time anymore. Therefore, time evolution becomes meaningless, and even if you try to evolve by treating the t coordinate as time, every mode will be exponentially growing. Therefore, similar to gradient instability, there is no limit to the growth rate. This type of instability is called "ghost" instability.

In our basic model, when two instabilities are present simultaneously, they can be considered as being equivalent to the third instability. This is due to the fact that one multiplies the action by -1 and gets the same theory. Though this is not necessarily the case, as we will see in the following discussions, e.g., in scalarization, Eq. (2.14), the scalar field is coupled to other fields; hence overall sign matters. Therefore, we will categorize each instability in our analysis.

4.2 Vectorization

We have already explained how one can generalize the idea of scalarization to vectorization in Sec. 2.3. Now, we will see in detail here how one can find vectorized solutions starting from the Action 2.26. To start with, let us rewrite the equation for the vector field given in Eq. (2.27) in the following form

$$\nabla_\mu F^{\mu\nu} = \hat{z} m_V^2 X^\nu \, , \tag{4.7}$$

where we defined

$$\hat{z} = 1 - \frac{8\pi}{m_V^2} \frac{\mathrm{d} \ln \mathcal{A}}{\mathrm{d}\mathfrak{x}} \mathcal{A}^4 \tilde{T} \, . \tag{4.8}$$

And let us write down the modified Einstein Field Equations as well

$$R_{\mu\nu} = 8\pi \left(T_{\mu\nu} - \frac{1}{2} T g_{\mu\nu} \right) + 2F_{\mu\alpha} F^{\alpha}_{\ \nu} - \frac{1}{2} F_{\alpha\beta} F^{\alpha\beta} g_{\mu\nu} + 2m_V^2 X_\mu X_\nu \, , \tag{4.9}$$

where $\tilde{T}$ is the trace of the energy-momentum tensor in the Jordan frame, which for a perfect fluid $\tilde{T} = -\tilde{\rho} + 3\tilde{p}$ where $\tilde{\rho}$ is the rest frame energy density and $\tilde{p}$ is the pressure of the fluid. For non-relativistic fluid, pressure is negligible. Hence, $\tilde{T} \approx -\tilde{\rho} < 0$. Similar to the DEF model, Choosing a suitable $\mathcal{A}$, e.g. $\mathcal{A} = e^{\beta_V \mathfrak{X}^2/2}$ with $\beta_V < 0$, m_{eff} can be negative and triggers tachyonic instability. For the case of NSs, as we will see, this is precisely the situation; the order of unity values of β_V can lead to vectorized NS solutions. If we assume spherically symmetric and static metric

$$\mathrm{d}s^2 = -e^{\nu}(r)\,\mathrm{d}t^2 + \frac{1}{1-\frac{2\mu(r)}{r}} + r^2\,\mathrm{d}\Omega^2 \tag{4.10}$$

and energy-momentum tensor for a perfect fluid in the Jordan frame

$$\tilde{T}^{\mu\nu} = (\tilde{p}+\tilde{\rho})\tilde{u}^{\mu}\tilde{u}^{\nu} + \tilde{p}\tilde{g}^{\mu\nu}\,, \tag{4.11}$$

where $\tilde{u}^{\mu}$ is the 4-velocity of the fluid. We can also write, without loss of generality,

$$X^{\mu} = (X^0(r), 0, 0, 0) = X^0(r)\partial_0\,. \tag{4.12}$$

To see why this is true, consider Eq. (4.9). The spherical symmetry in the metric implies the Ricci tensor is diagonal. Therefore from the last term, we can deduce that there is only one nonzero component. Furthermore, we have $R_{\phi\phi} = \sin^2\theta R_{\theta\theta}$ which means θ and ϕ components are zero. Finally, looking at the r component of the Eq (4.7) and using the divergence formula for an anti-symmetric tensor, we can see that

$$X^r = \frac{\partial_\rho(\sqrt{-g}F^{\alpha r})}{\sqrt{-g}(-4\pi\mathcal{A}^4\beta_V\tilde{T} + m_V^2)} = 0\,, \tag{4.13}$$

hence, the only nonzero term is X^0 as in Eq. (4.12). Then, we define new variables for convenience, namely, $\Phi = -n^{\mu}X_{\mu} = -e^{-\nu/2}$ and $E = (\partial_r^{\mu} + n^{\mu}n_r)F_{\mu\nu}n^{\nu} = e^{-\nu/2}\partial_r X_0$, where $n_{\mu} = (-e^{\nu/2}, 0, 0, 0)$ is the normal vector to the constant time hypersurfaces. In the end, in light of these assumptions and in terms of these

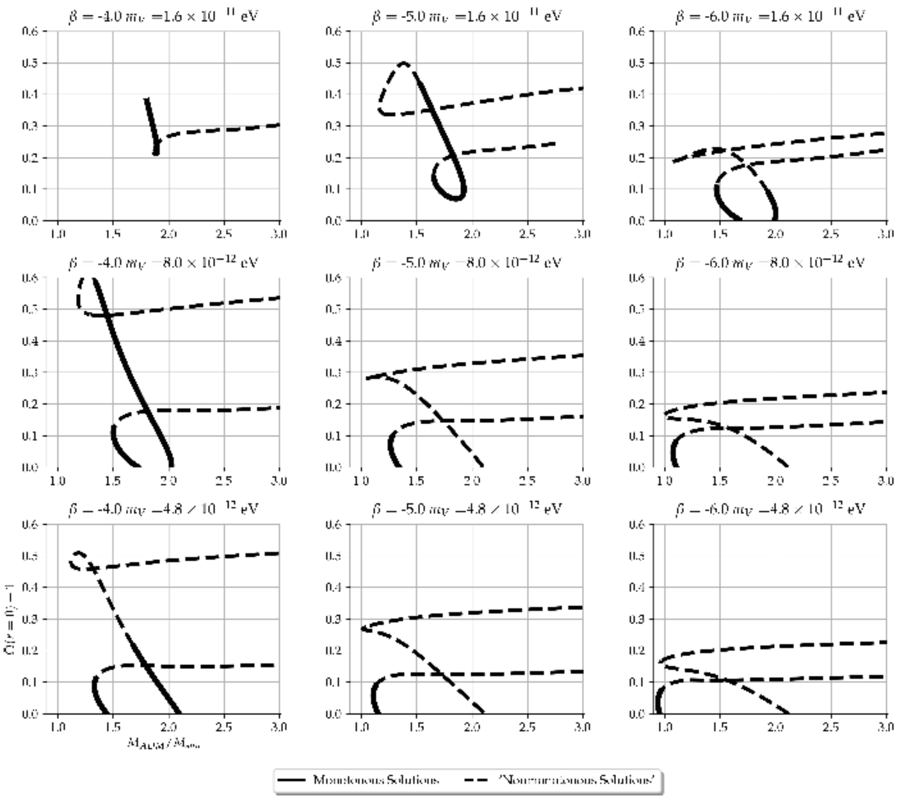

Figure 4.1: Strength of vectorization measured by $\mathcal{A}(r = 0) - 1$ vs Mass of the NSs. Solutions found by numerically solving the system of ODEs given in Eqs. (4.14). Dashed lines represent the solutions with monotonous behavior in either vector field, central density, or pressure, while the solid lines are the monotonous solutions.

variables, the modified TOV equations take the following form:

$$
\begin{aligned}
\mu' &= r^2 \left[4\pi \mathcal{A}_X^4 \tilde{\rho} - 8\pi \mathcal{A}_X^4 \Lambda(-\tilde{\rho} + 3\tilde{p})\Phi^2 + \frac{1}{2}(1 - \frac{2\mu}{r})E^2 + \frac{1}{2} m_V^2 \Phi^2 \right] \\
\nu' &= \frac{r^2}{r - 2\mu} \left[8\pi \mathcal{A}_X^4 \tilde{p} - (1 - \frac{2\mu}{r})E^2 + m_V^2 \Phi^2 + \frac{2\mu}{r^3} \right] \\
\Phi' &= -\frac{\nu'}{2}\Phi - E \\
E' &= \frac{1}{r - 2\mu} \left\{ \left[-2 + 3\mu/r + \mu' \right] E - \left[m_V^2 - 8\pi A_X^4 \Lambda(-\tilde{\rho} + 3\tilde{p}) \right] r\Phi \right\} \\
\tilde{p}' &= -(\tilde{\rho} + \tilde{p}) \left[\nu'/2 - 2\Lambda\Phi\Phi' \right]
\end{aligned}
\tag{4.14}
$$

Vectorized solutions are found by numerically solving the Eqs. (4.14) for different values of m_V and β_V. The value $\mathcal{A}(r = 0) - 1$ is determined as the strength of vectorization for each solution and plotted against the mass of the NS in Fig.4.1 for $\beta < 0$ and in Fig. 4.2. The first thing to notice in these plots is the fact that, unlike scalarization, there is no pattern in the figures. For the scalarization, it is known that the scalarized solutions continuously merge with the GR solutions as $\beta \to 0$, whereas here, we see no such trend.

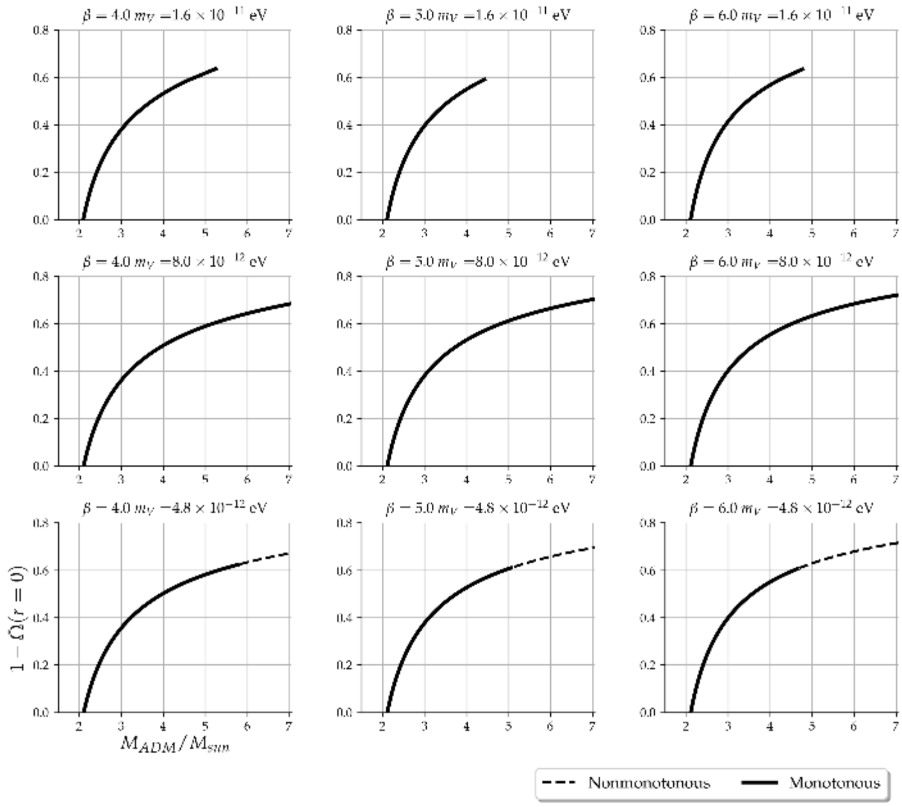

Figure 4.2: Same as Fig. 4.1 but for $\beta > 0$.

The vectorization mechanism indeed looks pretty similar to the scalarization. However, a quick overview of Fig. 4.1 tells us an essential message, the scalarization and vectorization are not exactly the same, and one can suspect the stability of these solutions. One other major difference between vectorization and scalarization is the degrees of freedom. Coupling the scalar field with the curvature brings another additional degree of freedom to the theory. For vectorization, on the other hand, the additional degrees of freedom become 3. As we will discuss in the next chapter, these additional degrees of freedom are indeed problematic since they do not only contain tachyonic instabilities but ghosts as well.

4.3 Perturbative analysis

This section will follow the discussions on Refs. [33, 34]. First, we will investigate the solutions with the GR background and perform a perturbative analysis. This will reveal that all such solutions contain ghost instabilities. Then, we will investigate the idea of eliminating these pathologies by performing a similar analysis for the solutions with vectorized backgrounds. We will also see that these solutions are not physical, i.e., ghosts.

4.3.1 Ghost and gradient instabilities in GR background

Let us start our discussion by taking the derivative of both sides in Eq. (4.7)

$$\nabla_\mu \nabla_\nu F^{\mu\nu} = \nabla_\mu (\hat{z} m_V^2 X^\mu) \tag{4.15}$$

Since $F^{\mu\nu}$ is antisymmetric, we have $\nabla_\mu \nabla_\nu F^{\mu\nu} = 0$. Therefore, we get

$$\nabla_\mu (\hat{z} X^\mu) = 0 \,, \tag{4.16}$$

which is called generalized Lorenz condition [33]. This can be recast into the following form

$$\partial_0 (\sqrt{-g}\hat{z} X^0) = -\partial_i (\sqrt{-g}\hat{z} X^i) \tag{4.17}$$

where i runs over the space coordinates. This equation is a time evolution for X^0 and contains divergent terms, as we will explain shortly. However, notice that X^0 is not a dynamical degree of freedom since the action does not contain its time derivative. The zeroth component of the field equation (4.7) is not an evolution equation but an elliptic constrain equation [64]. Nonetheless, it is possible to indirectly determine the time evolution of X^0 from the dynamics of other related variables, which can be derived from the constraint equation [17, 33].

We see that $\hat{z} = 1$ when $\tilde{T} = 0$, e.g., outside the neutron star. But we also need $\hat{z} < 0$ for vectorized solutions, meaning that $\hat{z}$ crosses zero at some point since it is continuous. However, since the derivative of the $\hat{z}$ might still be nonzero at that point, $\sqrt{-g}\hat{z}X^0$ might not vanish as well. Therefore, in general, X^0 will diverge.

Let us first recast the vector field equation (4.7) into an explicitly hyperbolic form to see that this instability is indeed related to a ghost instability. To achieve this, let us rewrite the constrain equation (4.16) as

$$\nabla_\mu X^\mu = -X^\mu \nabla_\mu \ln|\hat{z}| \tag{4.18}$$

Next, we modify Eq. (4.7) in the following manner

$$\begin{aligned} \hat{z} m_V^2 X_\nu =& \nabla_\mu F^\mu_{\ \nu} , \\ =& \nabla_\mu \nabla^\mu X_\nu - \nabla_\mu \nabla^\nu X^\mu , \\ =& \Box X_\nu - \nabla_\nu \nabla_\mu A^\mu - R^\mu_{\ \alpha\mu\nu} X^\alpha , \\ =& \Box X_\nu + \nabla_\nu (X^\mu \nabla_\mu \ln|\hat{z}|) - R_{\nu\mu} X^\mu , \end{aligned} \tag{4.19}$$

where we used the Reimann tensor's definition as a commutator of two covariant derivatives in the third line and plugged in Eq. (4.18) in the fourth line. The resulting equation is

$$\Box X_\nu + (\nabla_\mu \ln|\hat{z}|) \nabla_\nu X^\mu = \mathcal{M}_{\nu\mu} X^\mu \tag{4.20}$$

where we defined a mass-squared tensor

$$\mathcal{M}_{\alpha\beta} = \hat{z} m_V^2 g_{\alpha\beta} + R_{\alpha\beta} - \nabla_\alpha \nabla_\beta \ln|\hat{z}| \, . \tag{4.21}$$

This equation can be seen as the generalized massive wave equation where the principle part, in other words, the highest derivative term is $\Box X_\nu$ [2]. Notice the term $\nabla_\alpha \nabla_\beta \ln|\hat{z}|$ in Eq. (4.21) which contains powers of $\hat{z}^{-1}$. Hence, when $\hat{z}$ vanishes, the effective mass-squared tensor diverges. Alternatively, when we move the $\hat{z}^{-1}$ terms to the left-hand side, the principal part becomes $\hat{z}\Box X_\nu$, i.e. the dynamics of X^μ is governed by an effective metric defined as

$$\breve{g}^{\mu\nu} \equiv \hat{z} g^{\mu\nu} \, . \tag{4.22}$$

[2] Note that $\hat{z}$ also contains X^ν, therefore seems like it belongs to the principal part as well. However, for the perturbative values of X^ν, this dependence can be neglected to the leading order.

We know that $\hat{z}$ vanishes at some point from our previous discussion. Hence, the signature of the effective metric changes when $\hat{z}$ changes sign. In other words, if $\breve{g}^{00}$ becomes positive, there is a ghost instability, and if $\breve{g}^{ii}$ becomes negative, there is a gradient instability (see Sec. 4.1). Though, the situation is a bit different for the massless vectors, i.e., when $m_V = 0$, the Eq. (4.8) gets modified and may cross zero since it is expected to be negative inside and zero outside the star. However, a detailed analysis shows that the theory suffers from ghost instability even in that case. See Appendix A.

An alternative way to see the ghost nature of the dynamics in this model is by considering the following substitution to the action (2.26), which is known as the Stueckelberg trick [65]

$$X_\mu \longrightarrow X_\mu + {m_V}^{-1}\nabla_\mu\psi \ . \tag{4.23}$$

Then, the action (2.26) becomes

$$\begin{aligned} S =& \frac{1}{16\pi}\int \mathrm{d}^4x\sqrt{-g}\left[R - F_{\mu\nu}F^{\mu\nu} - 2g^{\mu\nu}\Big(m_V X_\mu + \nabla_\mu\psi\Big)\Big(m_V X_\nu + \nabla_\nu\psi\Big)\right] \\ &+ S_\mathrm{m}\Big[\Psi_\mathrm{m};\, \mathcal{A}^2(X_\alpha, \nabla_\alpha\psi)g_{\mu\nu}\Big], \end{aligned} \tag{4.24}$$

and the conformal function takes the form

$$\ln\mathcal{A} = \frac{\beta}{2m_V^2}g^{\mu\nu}(m_V X_\mu + \nabla_\mu\psi)(m_V X_\nu + \nabla_\nu\psi). \tag{4.25}$$

We see that this action is gauge invariant under the following transformations

$$X_\alpha \longrightarrow X_\alpha + \nabla_\alpha\lambda, \qquad \psi \longrightarrow \psi - m_V\lambda\ , \tag{4.26}$$

hence, we can set $\psi = 0$ by a suitable choice of λ. In other words, The action (2.26) is a gauge fixed version of the action (4.24). Now, if we vary the action with respect to the scalar field ψ, we get the following equation of motion

$$\Box\psi = -m_V\nabla_\mu X^\mu + \frac{4\pi}{m_V}\nabla_\mu\Big(\alpha^\mu_\mathrm{A}\mathcal{A}^4\tilde{T}\Big), \tag{4.27}$$

where we defined

$$\alpha^\mu_\mathrm{X} \equiv \frac{\partial\ln\mathcal{A}}{\partial X_\mu} = m_V\frac{\partial\ln\mathcal{A}}{\partial(\nabla_\mu\psi)} = \frac{\beta}{m_V}(m_V X^\mu + \nabla^\mu\psi). \tag{4.28}$$

This equation can be recast into the following form by using the effective metric definition we did in Eq. (4.22)

$$\breve{\Box}\psi = -\breve{g}^{\mu\nu}[m_V\breve{\nabla}_\mu X_\nu + \tfrac{1}{2}(\breve{\nabla}_\mu \ln \hat{z})(\breve{\nabla}_\nu\psi + m_V X_\nu)]. \tag{4.29}$$

Similar to our previous discussion, the dynamics of this equation are indeed problematic due to the behavior of $\hat{z}$, which determines the signature of the metric $\breve{g}$. Therefore, there is a ghost or gradient instability where the components of the metric change sign. In particular, there is a ghost if $\breve{g}^{00} > 0$ and gradient instability if $\breve{g}^{ii} < 0$.

These analyses clearly show the problematic behavior of vectorization. However, there might be a possible solution if one can effectively control the ghost instability through nonlinear means, akin to how the tachyonic instability in scalarization can be suppressed. In principle, if a nonlinear quenching mechanism is in place, it can potentially suppress the ghost instability. However, as we shall see in the following chapter, vectorized solutions contain ghost instabilities just as the GR solutions contain, as we showed here.

4.3.2 Ghost and gradient instabilities in vectorized solutions

In this section, we will generalize the analysis we introduced on the GR solutions in the previous section to the vectorized solutions. Therefore, in a similar manner, we will start by looking at the Lorenz constraint, but this time for a fixed vectorized background rather than a GR background. Consider the following perturbation of the vector field around a vectorized solution

$$X^\mu = \bar{X}^\mu + \delta X^\mu \ , \tag{4.30}$$

where overbar means the exact vectorized solution from now on. Then, the Lorenz condition given in Eq. (4.16) takes the following form

$$\overline{\nabla}_\mu(\Xi^\mu{}_\nu \delta X^\nu) = 0 \ , \tag{4.31}$$

where we defined

$$\Xi^\mu{}_\nu \equiv \bar{z}\delta^\mu{}_\nu + 2\overline{\frac{\mathrm{d}\hat{z}}{\mathrm{d}(X^\alpha X_\alpha)}}\bar{X}^\mu \bar{X}_\nu \ . \tag{4.32}$$

We choose the conformal factor to be $\mathcal{A} = e^{\beta_V X^\alpha X_\alpha/2}$ similar to our previous discussion. Hence, we get the following

$$m_V^2\, \Xi^\mu{}_\nu = -16\pi\beta_V^2 \tilde{T}_{\rm vec} e^{2\beta_V \bar{X}^\rho \bar{X}_\rho}\, \bar{X}^\mu \bar{X}_\nu + \left(m_V^2 - 4\pi\beta_V \tilde{T}_{\rm vec} e^{2\beta_V \bar{X}^\rho \bar{X}_\rho}\right)\delta^\mu{}_\nu\,, \quad (4.33)$$

or writing out explicitly

$$\Xi^0{}_0 = 1 - \frac{4\pi\beta_V \tilde{T}_{\rm vec} e^{2\beta_V \bar{X}^0 \bar{X}_0}\left(1 + 4\beta_V \bar{X}^0 \bar{X}_0\right)}{m_V^2} \quad (4.34)$$

$$\Xi^i{}_i = 1 - \frac{4\pi\beta_V \tilde{T}_{\rm vec} e^{2\beta_V \bar{X}^0 \bar{X}_0}}{m_V^2} \quad \text{(no sum)}\,, \quad (4.35)$$

where $\tilde{T}_{\rm vec}$ is the trace of the stress-energy tensor for the vectorized background, and there is no summation over i. In other words, the $\Xi^\mu{}_\nu$ is diagonal due to the form of the vector field and the metric, which allows us the write down the Eq. (4.31) in the following form

$$\partial_0\left(\sqrt{-\bar{g}}\; \Xi^0{}_0 \delta X^0\right) = -\sum_{i=1}^{3} \partial_i\left(\sqrt{-\bar{g}}\; \Xi^i{}_i \delta X^i\right)\,. \quad (4.36)$$

Notice the similarity between the Eq. (4.17). Therefore, in a similar fashion, we run into problems of the same sort if we have a point where $\Xi^0{}_0 = 0$. In other words, there is no symmetry to ensure that the right-hand side will also vanish at the same point. Therefore, we have divergent terms in Eq. 4.36. Of course, we don't know for sure yet that the condition that $\Xi^0{}_0$ crosses zero is generally satisfied, which wasn't the case for $\hat{z}$. However, let us first analyze the nature of instability, and later on, we will see that this condition is indeed satisfied for all vectorized solutions.

To see that this instability is related to a ghost instability, we perform the Stueckelberg trick introduced in Eq. (4.23) following the Refs. [17, 33]. This time, instead of varying the action and looking at the equations of motion, let us take a short way and directly substitute Eq.(4.23) into Lorenz constrain (4.18). This results in the following modified Lorenz condition

$$\nabla_\mu\left[\hat{z}\left(X_\mu + \frac{1}{m_V}\nabla_\mu \psi\right)\right] = 0\,. \quad (4.37)$$

Perturbing the vector field around the vectorized solution as in Eq. (4.30) yields

$$\bar{\nabla}_\mu \left[\Xi^{\mu\nu} \left(\delta X_\nu + \frac{1}{m_V} \bar{\nabla}_\nu \delta\psi \right) \right] = 0, \tag{4.38}$$

where

$$\Xi^{\mu\nu} = \bar{g}^{\nu\rho} \Xi^\mu{}_\rho = \bar{z}\, \bar{g}^{\mu\nu} + 2\, \overline{\frac{\mathrm{d}\hat{z}}{\mathrm{d}(X^\alpha X_\alpha)}}\, \bar{X}^\mu \bar{X}^\nu . \tag{4.39}$$

The principle part of the Eq. (4.38), the highest derivative term is $\Xi^{\mu\nu}\bar{\nabla}_\mu\bar{\nabla}_\nu\delta\psi$. Therefore, $\Xi^{\mu\nu}$ acts as an effective inverse metric and determines the evolution of $\delta\psi$. In other words, similar to Eq. (4.22) if we define

$$\breve{g}^{\mu\nu} \equiv \Xi^{\mu\nu} \tag{4.40}$$

the equations of motion take the following form

$$\breve{\Box}\delta\psi = -m_V \breve{\nabla}_\alpha \delta X^\alpha + \Delta\Gamma^\beta_{\alpha\rho} \Xi^{\sigma\rho} \left(m_V \delta X_\sigma + \breve{\nabla}_\sigma \delta\psi \right) \tag{4.41}$$

where $\breve{\Box}$ and $\breve{\nabla}$ are operators on $\breve{g}^{\mu\nu}$ and $\Delta\Gamma^\mu_{\alpha\beta} \equiv \breve{\Gamma}^\mu_{\alpha\beta} - \Gamma^\mu_{\alpha\beta}$. Therefore, analogous to our argument in the previous section, a positive value of $\breve{g}^{00}$ implies a ghost instability and a negative value of $\breve{g}^{ii}$ implies gradient instability (see Sec. 4.1). Notice that the sign change in $\Xi^0{}_0$ implies a sign change in Ξ^{00} or equivalently in $\breve{g}^{00}$ since both the metric and $\Xi^\mu{}_\nu$ are both diagonal. Therefore, the divergence in Eq. (4.31) occurs exactly when $\delta\psi$ becomes a ghost.

Finally, let us also show the ghost nature in the dynamics of the theory without invoking the Stueckelberg trick. Remember how we manipulated the vector field equation in Eq.(4.19) and ended up with the generalized massive wave equation given in Eq. (4.20). Now, following the same steps for a spherically symmetric vectorized background, the subsequent term additionally plays a role in the principle part of the equation

$$\bar{\nabla}_\alpha \bar{\nabla}_\beta \ln \hat{z} = \frac{2}{\bar{z}} \overline{\frac{d\hat{z}}{d(A^\rho X_\rho)}} \bar{X}^\sigma \bar{\nabla}_\alpha \bar{\nabla}_\beta \delta X_\sigma + \ldots \tag{4.42}$$

Hence, It is not trivial that the dynamics of δX^μ are governed by the effective metric in Eq. (4.40). However, since we know that only the nonzero component of the vector $\bar{X}_\mu$ is the 0 component, the principle part of the Eq. (4.20) for $\nu = 0$ becomes

$$\breve{g}^{\mu\nu}\partial_\mu\partial_\nu\delta X_0 \,. \tag{4.43}$$

In other words, the dynamics of δX_0 is governed by the effective metric $\breve{g}^{\mu\nu} = \Xi^{\mu\nu}$.Hence, it results in ghost instability when $\breve{g}^{00}$ becomes positive and gradient instability when $\breve{g}^{ii}$ becomes negative, which are the same conditions we found for the scalar field ψ.

Our analysis primarily concentrates on the direct extension of the DEF model mentioned in Ref. [17] whose action is given in Eq. (2.26). However, any vectorization model that features perturbation equations in the form of

$$\nabla_\mu F^{\mu\nu} = \Xi^\nu{}_\mu X^\mu \,, \tag{4.44}$$

will be applicable to certain outcomes of our study, such as Refs. [66–68]. However, it is important to acknowledge that the presence of nondiagonal terms, typically encountered in situations deviating from spherical symmetry, adds complexity to the analysis [69].

To sum up, our analysis has revealed that the presence of ghost or gradient instabilities is contingent upon the behavior of $\Xi^{\mu\nu}$, which functions as an effective metric for certain degrees of freedom of the action (2.26). A change in the sign of Ξ^μ_ν arises precisely under the same conditions as a change in the sign of $\Xi^{\mu\nu}$ since the signature of $g^{\mu\nu}$ is always $(-1, 1, 1, 1)$, as was previously mentioned. Therefore in Section 4.4, we will numerically compute Ξ^μ_ν profiles to determine the stability of each vectorized solution.

4.3.3 Tachyonic instabilities in vectorized solutions

Initially, vectorization was introduced to imitate the spontaneous growth of scalar field utilizing tachyon-based mechanisms [17]. In this case, the nonlinear effects restrain the instabilities as the field grows [9]. Having a ghost or gradient instability in a solution is enough to conclude that such a solution is not physical. However, it is still interesting to look at whether such unstable solutions also fail from tachyonic instability. In other words, we will investigate the nonlinear suppression of tachyonic instability in vectorized solution to see whether the tachyonic instability can be quenched or not.

To this end, following the Ref. [34], we will repeat a similar analysis to the one in Sec. 2.1 for the scalar field. Though, this time, we have ghost and gradient instabilities as well. This means that there exist divergent terms, and we cannot approach the problem perturbatively. However, we will assume that meaningful solutions exist and analyze the tachyonic modes. We start by decomposing the vector field perturbations around a vectorized background into spherical harmonics as

$$\delta X_\alpha = \frac{1}{r}\sum_{i=1}^{4}\sum_{\ell m} c_i u_{(i)}^{\ell m}(t,r) Z_\alpha^{(i)\ell m}(\theta,\phi), \tag{4.45}$$

where $c_3 = c_4 = 1/\sqrt{\ell(\ell+1)}$, $c_1 = c_2 = 1$ and

$$Z_\alpha^{(1)\ell m} = [1,0,0,0]Y_{\ell m}, \tag{4.46}$$

$$Z_\alpha^{(2)\ell m} = [0,1,0,0]Y_{\ell m}, \tag{4.47}$$

$$Z_\alpha^{(3)\ell m} = \frac{r}{\sqrt{\ell(\ell+1)}}[0,0,\partial_\theta,\partial_\phi]Y_{\ell m}, \tag{4.48}$$

$$Z_\alpha^{(4)\ell m} = \frac{r}{\sqrt{\ell(\ell+1)}}[0,0,\csc\theta\partial_\phi,-\sin\theta\partial_\theta]Y_{\ell m}, \tag{4.49}$$

with $Y_{\ell m}$ is the scalar spherical harmonics (for details see. [33, 70]). Under parity transformation, $\mathbf{x} \longrightarrow -\mathbf{x}'$, or in spherical coordinates $\theta \longrightarrow \pi - \theta$ and $\phi \longrightarrow \phi + \pi$, the first three of the above harmonics take a factor of $(-1)^\ell$ while the fourth one takes a factor of $(-1)^{\ell+1}$. For this reason, the former is called the "even-parity" mode, and the latter is called the "odd-parity" mode.

We focus on the odd-parity sector, which only has a single degree of freedom $u_4 \equiv u_{(4)}^{\ell 0}$ where we take $m = 0$ due to the spherical symmetry of the background. This mode is also called the "axial mode," and it behaves similarly to the case where the vector field vanishes due to $\bar{X}^\nu$ not having any angular component. Specifically, the action (2.26), up to quadratic terms in u_4, takes the following form after integrating over the angular part

$$S_{\mathrm{t}} = \int \mathrm{d}t\,\mathrm{d}r \frac{e^{\bar{\nu}/2}\left(1-2\bar{\mu}/r\right)^{-1/2}}{4\pi\ell(\ell+1)} \left\{ e^{-\bar{\nu}}(\dot{u}_4)^2 - \left(1-\frac{2\bar{\mu}}{r}\right)(u_4')^2 - \left(\frac{\ell(\ell+1)}{r^2} + \bar{z}m_V^2\right)u_4^2 \right\} \tag{4.50}$$

The equation of motion is the following

$$\left[-e^{-\bar{\nu}}\partial_t^2 + e^{-\bar{\nu}/2}\sqrt{1-\frac{2\bar{\mu}}{r}}\,\partial_r\left(e^{\bar{\nu}/2}\sqrt{1-\frac{2\bar{\mu}}{r}}\,\partial_r\right) - \frac{\ell(\ell+1)}{r^2} - \bar{z}m_V^2\right]u_4 = 0\,. \tag{4.51}$$

With the change of variable as $u_4(t,r) = e^{i\omega t}u(r)$, it becomes

$$\left[-\frac{d^2}{dr_*^2} + V_{\mathrm{eff}}(r)\right]u = \omega^2\,u\,, \tag{4.52}$$

where we defined the following transformations

$$\frac{dr_*}{dr} = e^{-\bar{\nu}/2}\left(1-\frac{2\bar{\mu}}{r}\right)^{-1/2} \tag{4.53}$$

$$V_{\mathrm{eff}}(r) = e^{\bar{\nu}}\left(\frac{\ell(\ell+1)}{r^2} + \bar{z}m_V^2\right)\,. \tag{4.54}$$

In this setup, if there is a solution to the eigenfunction problem in Eq. (4.52) satisfying $\omega^2 < 0$, then there exists a tachyonic instability.

It is important to note that the axial mode is defined for $\ell \geq 1$. Also, increasing ℓ contributes to V_{eff} in a positive manner making the mode less tachyonic. Hence, it is enough to check only $\ell = 1$ mode for the search for tachyon. If $V_{\mathrm{eff}} > 0$ everywhere, there is no tachyon in the axial sector since $\omega^2 > 0$ in this case due to the expectation value of the operator on the left-hand side is always positive.

All the analysis above is for the odd sector of the harmonics, and we cannot say anything regarding the even sector, $u_{1,2,3}$. In other words, we can show the existence of the tachyon from Eq. (4.52), but a negative result for u_4 does not necessarily mean that there is no tachyon in $u_{1,2,3}$. We will not delve into the details of the even sector as we shall see in the next section; they are already afflicted with ghost or gradient instabilities.

4.4 Results

Here we present the results of our numerical calculations from Ref. [34]. As mentioned in the previous sections, we recomputed the vectorized solutions given in [17] and some more by expanding our parameter space. We used the same numerical tools as in Chapter 3, checked the convergence, and performed independent residual. For our purposes, we calculated the $\Xi^{\mu}{}_{\nu}$ (Eq. (4.34) and Eq. (4.35))and V_{eff} (Eq. (4.54)) for each vectorized star using HB equation of state defined in [71].

We separated the solutions into two categories: "monotonic" and "non-monotonic" stars. The naming refers to the behavior of A_0 and $\tilde{\rho}$ profiles in stars. In particular, if there is an increase in either A_0 or $\tilde{\rho}$, we refer to them as "non-monotonic" and vice versa. We should note that even though the non-monotonicity is a sign of instability, we can't conclude the ends state just by this feature. Hence, we investigated all the vectorized solutions.

Let us start by summarizing the findings of the previous section

- There exist a ghost instability if $\Xi^{0}{}_{0} < 0$ anywhere.
- There exist a gradient instability if $\Xi^{i}{}_{i} < 0$ anywhere.
- There exist a tachyonic instability if the Eq. (4.52) has a negative eigenvalue, $\omega^2 < 0$. Though, the opposite may not be true.

4.4.1 *Vectorization with $\beta < 0$*

As mentioned in Sec. 4.1, having all three instability simultaneously means stability. However, since the vector field o-couples the other fields in action (2.26), this does not apply to our case. Therefore, the above classification makes sense.

The general trend in vectorized stars was already mentioned in previous chapters and can be seen in Fig 4.1. We found that all the vectorized stars, in this case, contain both ghost and gradient instabilities. This is the first major result of this chapter. The severity of the ghost and gradient instabilities in the stars, indicated by the most negative values achieved by $\Xi^{\mu}{}_{\nu}$, can be observed in Fig. 4.4. It is evident that the value of $\Xi^{\mu}{}_{\nu}$ is significantly negative, which means that a small change in the structure of the star cannot recover the ghost or gradient instabilities. An example vectorized star with $\Xi^{\mu}{}_{\nu}$ and V_{eff} profiles can be seen in Fig. 4.3.

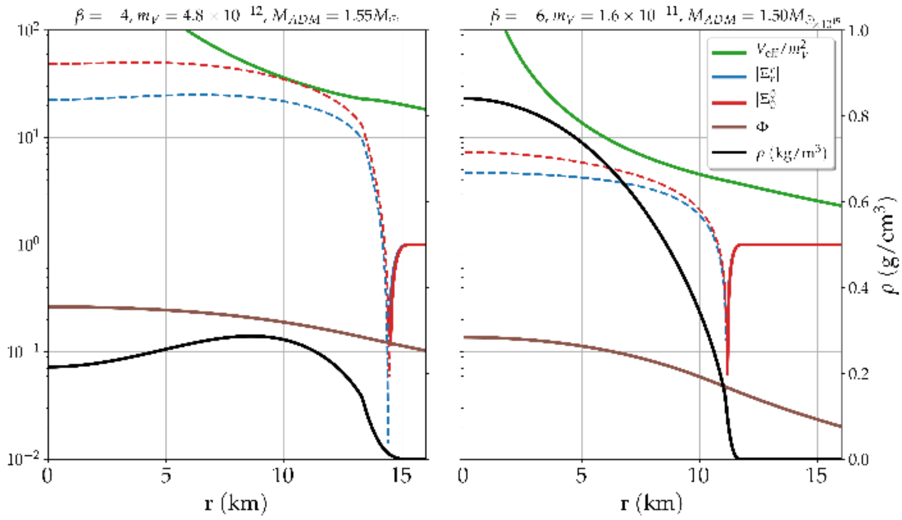

Figure 4.3: The logarithmic plots of the $\Xi^0{}_0$, $\Xi^r{}_r$, $V_{\rm eff}$, $\Psi = \sqrt{-X_0X^0}$ and $\tilde{\rho}$ profiles for a non-monotonic (left) and monotonic star for $\beta < 0$. Note that $\Xi^i{}_i$ is the same for all i's, Eq. (4.35). Ξ^0_0 and Ξ^r_r cut through zero, as can be seen as spikes in the figure. Dashed lines are places where functions attain negative values.

On the other hand, for the tachyonic instability, we see that $V_{\rm eff} > 0$ everywhere in monotonic stars and $V_{\rm eff} < 0$ only for a small portion in some non-monotonic stars. This means that u_4 mode is not tachyonic in the majority of the stars, but since we did not solve the eigenfunction problem in Eq. (4.52), we cannot conclude whether some have tachyons or not. Indeed, it might be the case that the tachyonic instability is suppressed by nonlinear terms for some, possibly all, solutions for u_4. But we should emphasize that irrespective of the outcome of the tachyon; there are ghost and gradient instabilities in all vectorized solutions. This alone is sufficient to classify the vectorized stars as unstable.

4.4.2 *Vectorization with $\beta > 0$*

Here we will repeat the same procedure of the previous section for $\beta > 0$. In earlier sections, we have shown that we can have vectorized solutions for $\beta > 0$. Now we will investigate the stability of such stars based on the criterion we introduced.

The general trend of such vectorized stars can be seen in Fig. 4.2 and sample

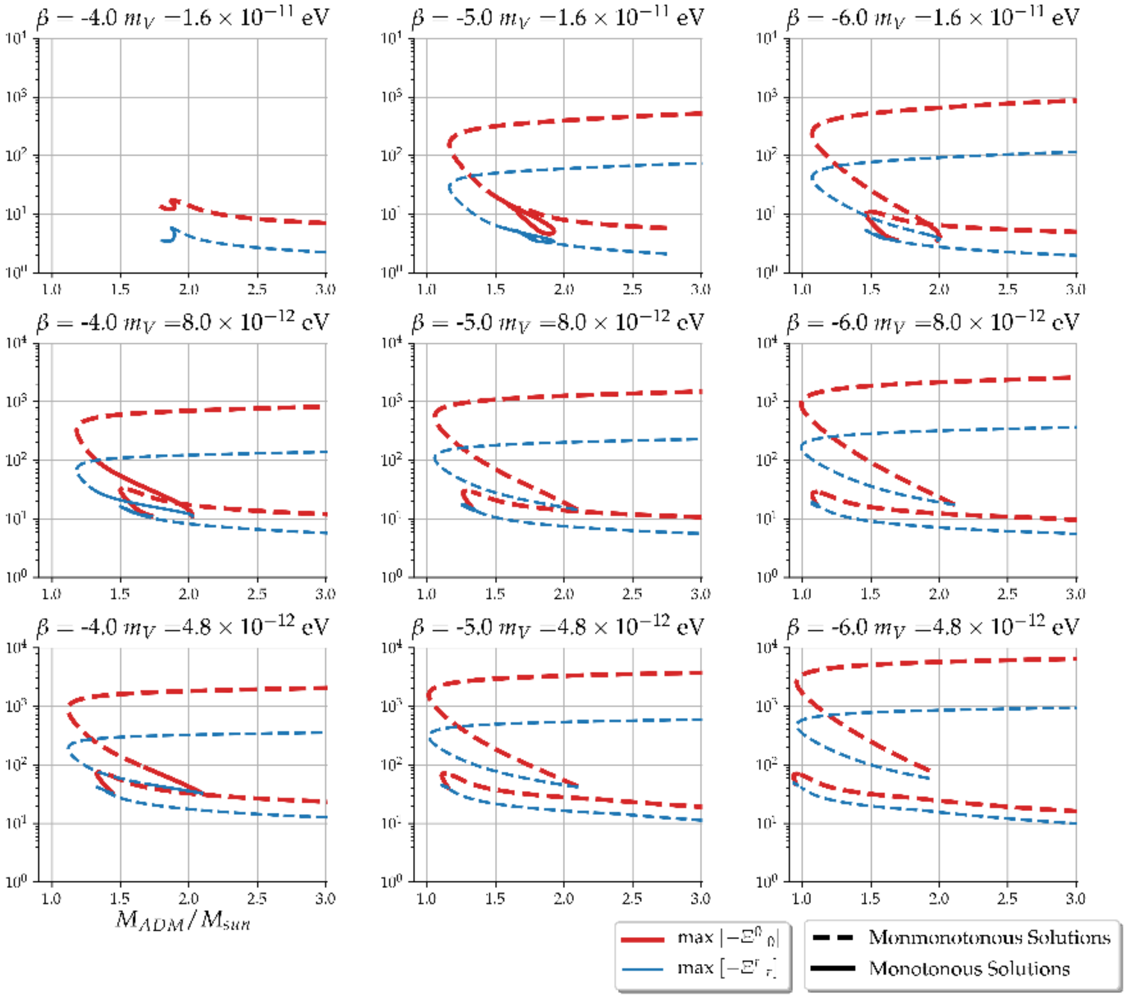

Figure 4.4: Maximum values of the $-\Xi^0{}_0$ and $-\Xi^r{}_r$ for $\beta < 0$, showing that negative values are present in all cases.

monotonic and non-monotonic stars in Fig. 4.5. One can also observe the behavior of $\Xi^\mu{}_\nu$ in Fig. 4.6 in a similar fashion to Fig.4.4. As can be verified from the values attained by $\Xi^\mu{}_\nu$, the same problem persists in all cases. All the vectorized stars have gradient instability. The majority of the solutions also have ghost instability though this time, some of the monotonic stars have $\Xi^0{}_0 > 0$ everywhere, indicating that they don't possess ghost instability. For the tachyonic instability, there are cases with both $V_{\text{eff}} > 0$ and $V_{\text{eff}} < 0$ for both monotonic and non-monotonic stars, but we do not further analyze since the fact that $\Xi^i{}_i < 0$ occurs in every solution is sufficient for concluding that all vectorized stars are unstable.

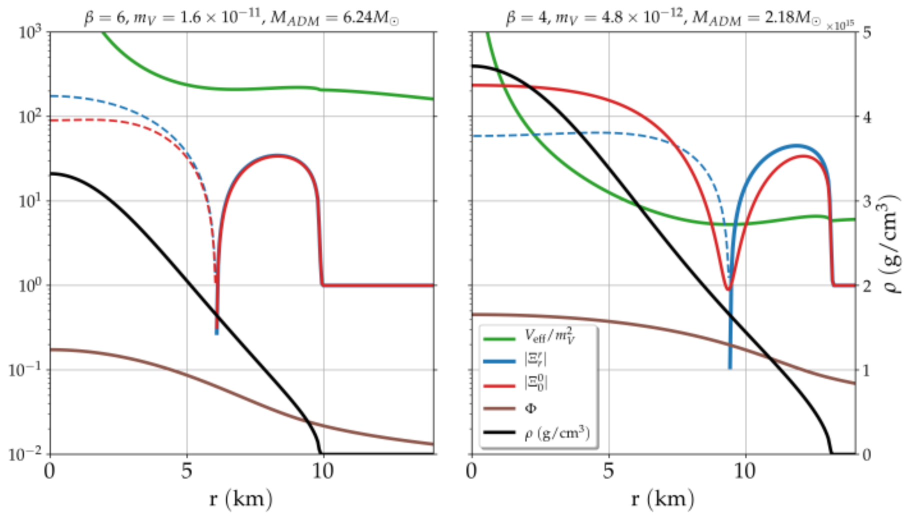

Figure 4.5: $\Xi^0{}_0$, $\Xi^r{}_r$, V_{eff}, $\Psi = \sqrt{-X_0 X^0}$ and $\tilde{\rho}$ profiles for a non-monotonic (left) and monotonic star, similar to 4.3 for $\beta > 0$

The instability is evident in all the solutions provided thus far, encompassing a wide range of (β, σ) values and ADM masses. This compellingly indicates that all static, spherically symmetric vectorized solutions are inherently unstable. Nevertheless, it is essential to acknowledge that we cannot definitively exclude the possibility of exceptions, as the parameter space is extensive. In the future, alternative numerical methods may be employed to explore additional regions of the parameter space [72].

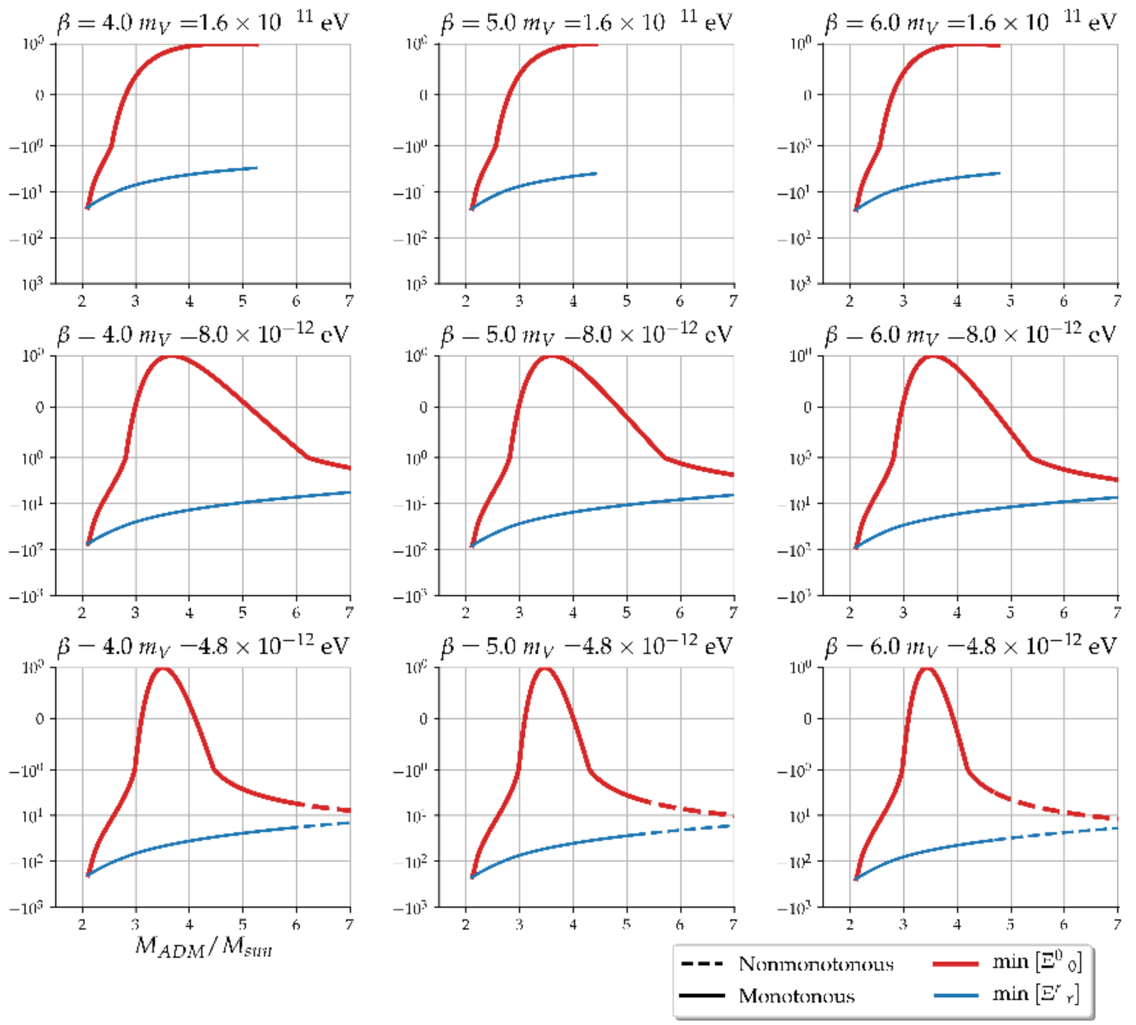

Figure 4.6: Similar to Fig. 4.4, maximum values of the $-\Xi^0_{\ 0}$ and $-\Xi^r_{\ r}$ for $\beta > 0$, showing that negative values are present for $\Xi^r_{\ r}$ in all cases, whereas for $\Xi^0_{\ 0} > 0$ sometimes. In other words, all solutions contain gradient instability, but some are ghost-free.

Chapter 5

DISCUSSION

We investigated the theoretical and observational ways of testing gravity theories with scalarization. We started by introducing the theory behind scalarization in Chapter. 2. Then, we moved to the observational tests for scalarization in Chapter 3 and explored the overall effectiveness of utilizing neutron star mass-radius measurements as a means to test theories of gravity. This methodology was already proved to be useful in constraining the original Damour and Esposito-Farèse model, which we called quadratic DEF [40]. Here, we showed that this is not a unique case, and the sGB model can also be constrained in a similar manner. However, our methodology was not successful in obtaining constraints for a modified version of the quadratic DEF model, the linear DEF model. Although the modification one imposes onto the theory is quite simple, it creates major differences between these two models.

First, the linear DEF model deviates considerably less from GR compared to quadratic DEF. We can question the effectiveness of our methodology by looking at this comparison only, but it is by all means not trivial. Despite being smaller, the deviations are still significant in absolute terms, as shown in Fig. 3.2. Second, and more importantly, while the amount of deviations increase in the limit $|\beta| \to \infty$ for the quadratic DEF, it tends to approach a certain value for the linear DEF. In other words, changing the theory parameter β barely changes the neutron star structure after some point in the linear DEF; hence, it is impossible to constrain using mass-radius data. However, there is a possibility that with more accurate data or improved methodology, constraints on the linear DEF model could be achieved in the future.

We also showed the effect of the dataset size on our findings. In particular, we demonstrated that even a slight increase in the number of measurements could drastically improve this methodology. These findings demonstrate that mass-radius data holds promise as a valuable tool for testing alternative theories of gravity. However, it is essential to acknowledge that there are clear limitations associated with its applicability.

One powerful side of this approach is that it can also constrain theory with a massive scalar field contrary to other observational bounds. For example, an observation of a pulsar-white dwarf binary put a very stringent bound on the theory with a massless scalar field [56]. Furthermore, there are cosmological reasons why the scalar field needs to attain a mass field [57]. However, our investigation of a massless scalar field is not in vain because we know that the theory continuously joins with GR as $m_\varphi \to 0$ [27]. This means that any bound we obtained is also viable for massive cases, similar to Ref. [40].

In the second part of this thesis, in Chapter 4, we theoretically investigated the generalization of the idea of scalarization to vector fields. In particular, we analyzed the theory in Ref. [17] and performed a perturbative analysis. Drawing an analogy with scalarization, it is anticipated that the vector field would undergo a tachyonic instability, which subsequently gets suppressed nonlinearly, and that this phenomenon is responsible for the emergence of vectorized configurations observed in earlier studies. On the contrary, a detailed investigation reveals the presence of ghosts and gradient instability [33] in these models. This outcome convincingly demonstrates that the apparent similarity between this vectorization model and the scalarization model of DEF is misleading. It becomes evident that there is no occurrence of a physically analogous phase transition process akin to scalarization. Potentially, one might expect nonlinear terms to effectively suppress the ghost instability, similar to how the tachyonic instability is quenched in scalarization [18]. However, in Chapter 4, by numerically computing the vectorized NSs, we have shown that all the vectorized solutions carry ghost or gradient instabilities. Therefore, there is no indication of any suppression or quenching of the instabilities [34]. Nevertheless, it is essential to note that, even if there were such a mechanism, the problem arises when one tries the evolve the system numerically. This is because we cannot make sense of a physical time evolution once there is ghost instability. Our findings were obtained through the investigation of the linearized vector field equations on a fixed vectorized neutron star background. We have demonstrated that the presence of instabilities correlates with the sign change in components of a tensor $\Xi_{\mu\nu}$.

The contrasting characteristics between the vectorized neutron star solutions illustrated in Fig. 4.1 and their scalarization counterparts have already raised concerns regarding the stability of the vectorized configurations. In the end, we have verified these concerns and uncovered the instabilities. The analysis provided in Chapter. 4 was specific to a single theory; however, any theory where the field equations contain the term $\nabla_\mu F^{\mu\alpha}$ as the principle part can be constrained in a similar manner [33]. There are other generalizations of scalarization [18, 31, 32]. The development of tools for conducting stability analyses of solutions within these theories represents a future area of interest.

It is important to emphasize that un-vectorized NS, i.e., $\beta_V = 0$, which corresponds to GR, is also a solution in this theory. And these solutions have also been shown to possess ghost and gradient instabilities. Therefore, the theory given in action (2.26) is not well-posed.

In summary, this thesis explored alternative gravity models, focusing on scalarization, and introduced observational and theoretical tests to study their validity. These tests are important in our pursuit of understanding the true nature of gravity and hopefully will shed light on future research.

BIBLIOGRAPHY

[1] B. P. Abbott *et.al* (LIGO Scientific Collaboration and Virgo Collaboration), "Observation of gravitational waves from a binary black hole merger," Phys. Rev. Lett. **116**, 061102 (2016).

[2] B. Bertotti, L. Iess, and P. Tortora, "A test of general relativity using radio links with the cassini spacecraft," Nature **425**, 374–376 (2003).

[3] C. M. Will, "The confrontation between general relativity and experiment," Living Reviews in Relativity **4**, 4 (2001).

[4] R. Abbott *el. al* (LIGO Scientific Collaboration and Virgo Collaboration), "Tests of general relativity with binary black holes from the second ligo-virgo gravitational-wave transient catalog," Phys. Rev. D **103**, 122002 (2021).

[5] R. Abbott *et. al* (LIGO Scientific Collaboration and Virgo Collaboration), "Gwtc-2: Compact binary coalescences observed by ligo and virgo during the first half of the third observing run," Phys. Rev. X **11**, 021053 (2021).

[6] C. Rovelli, *Quantum Gravity*, Cambridge Monographs on Mathematical Physics (Cambridge University Press, 2004).

[7] S. Bose, A. Mazumdar, G. W. Morley, H. Ulbricht, M. Toroš, M. Paternostro, A. A. Geraci, P. F. Barker, M. S. Kim, and G. Milburn, "Spin entanglement witness for quantum gravity," Phys. Rev. Lett. **119**, 240401 (2017).

[8] S. M. Carroll, *Spacetime and Geometry: An Introduction to General Relativity* (Cambridge University Press, 2019).

[9] T. Damour and G. Esposito-Farèse, "Nonperturbative strong-field effects in tensor-scalar theories of gravitation," Phys. Rev. Lett. **70**, 2220–2223 (1993).

[10] D. Lovelock and H. Rund, *Tensors, Differential Forms, and Variational Principles*, Dover Books on Mathematics (Dover Publications, 2012).

[11] D. D. Doneva, F. M. Ramazanoğlu, H. O. Silva, T. P. Sotiriou, and S. S. Yazadjiev, "Scalarization," (2022), arXiv:2211.01766 [gr-qc] .

[12] T. Clifton, *Alternative theories of gravity*, Other thesis (2006), arXiv:gr-qc/0610071 .

[13] T. Clifton, P. G. Ferreira, A. Padilla, and C. Skordis, "Modified Gravity and Cosmology," Phys. Rept. **513**, 1–189 (2012), arXiv:1106.2476 [astro-ph.CO] .

[14] D. D. Doneva and S. S. Yazadjiev, "New gauss-bonnet black holes with curvature-induced scalarization in extended scalar-tensor theories," Phys. Rev. Lett. **120**, 131103 (2018).

[15] L. Barack *et. al*, "Black holes, gravitational waves and fundamental physics: a roadmap," Classical and Quantum Gravity **36**, 143001 (2019).

[16] E. Berti *et. al.*, "Testing general relativity with present and future astrophysical observations," Classical and Quantum Gravity **32**, 243001 (2015).

[17] F. M. Ramazanoğlu, "Spontaneous growth of vector fields in gravity," Phys. Rev. D **96**, 064009 (2017).

[18] F. M. Ramazanoğlu, "Regularization of instabilities in gravity theories," Phys. Rev. D **97**, 024008 (2018).

[19] H. O. Silva, J. Sakstein, L. Gualtieri, T. P. Sotiriou, and E. Berti, "Spontaneous scalarization of black holes and compact stars from a gauss-bonnet coupling," Phys. Rev. Lett. **120**, 131104 (2018).

[20] D. D. Doneva and S. S. Yazadjiev, "Neutron star solutions with curvature induced scalarization in the extended gauss-bonnet scalar-tensor theories," Journal of Cosmology and Astroparticle Physics **2018**, 011 (2018).

[21] R. F. P. Mendes, "Possibility of setting a new constraint to scalar-tensor theories," Phys. Rev. D **91**, 064024 (2015).

[22] R. F. P. Mendes and N. Ortiz, "Highly compact neutron stars in scalar-tensor theories of gravity: Spontaneous scalarization versus gravitational collapse," Phys. Rev. D **93**, 124035 (2016).

[23] T. Harada, "Neutron stars in scalar-tensor theories of gravity and catastrophe theory," Phys. Rev. D **57**, 4802–4811 (1998).

[24] C. Palenzuela and S. L. Liebling, "Constraining scalar-tensor theories of gravity from the most massive neutron stars," Phys. Rev. D **93**, 044009 (2016).

[25] R. F. P. Mendes and N. Ortiz, "New class of quasinormal modes of neutron stars in scalar-tensor gravity," Phys. Rev. Lett. **120**, 201104 (2018).

[26] R. F. P. Mendes and T. Ottoni, "Scalar charges and pulsar-timing observables in the presence of nonminimally coupled scalar fields," Phys. Rev. D **99**, 124003 (2019).

[27] F. M. Ramazanoğlu and F. Pretorius, "Spontaneous Scalarization with Massive Fields," Phys. Rev. D **93**, 064005 (2016), arXiv:1601.07475 [gr-qc] .

[28] N. D. Birrell and P. C. W. Davies, *Quantum Fields in Curved Space*, Cambridge Monographs on Mathematical Physics (Cambridge Univ. Press, Cambridge, UK, 1984).

[29] E. S. Demirboğa, Y. E. Şahin, and F. M. Ramazanoğlu, "Subtleties in constraining gravity theories with mass-radius data," (2023), arXiv:2303.01910 [gr-qc] .

[30] C. F. B. Macedo, J. Sakstein, E. Berti, L. Gualtieri, H. O. Silva, and T. P. Sotiriou, "Self-interactions and spontaneous black hole scalarization," Phys. Rev. D **99**, 104041 (2019).

[31] F. M. Ramazanoğlu, "Spontaneous growth of spinor fields in gravity," Phys. Rev. D **98**, 044011 (2018).

[32] F. M. Ramazanoğlu, "Various paths to the spontaneous growth of p-form fields," Turkish Journal of Physics **43**, 596 (2019).

[33] H. O. Silva, A. Coates, F. M. Ramazanoğlu, and T. P. Sotiriou, "Ghost of vector fields in compact stars," Phys. Rev. D **105**, 024046 (2022).

[34] E. S. Demirboğa, A. Coates, and F. M. Ramazanoğlu, "Instability of vectorized stars," Phys. Rev. D **105**, 024057 (2022).

[35] B. P. Abbot *et. al.* (LIGO Scientific Collaboration and Virgo Collaboration), "Tests of general relativity with gw170817," Phys. Rev. Lett. **123**, 011102 (2019).

[36] S. Bogdanov *et. al*, "Constraining the neutron star mass–radius relation and dense matter equation of state with NICER. I. the millisecond pulsar x-ray data set," The Astrophysical Journal Letters **887**, L25 (2019).

[37] S. Bogdanov *et. al*, "Constraining the neutron star mass–radius relation and dense matter equation of state with NICER. II. emission from hot spots on a rapidly rotating neutron star," The Astrophysical Journal Letters **887**, L26 (2019).

[38] S. Bogdanov *et. al*, "Constraining the neutron star mass–radius relation and dense matter equation of state with NICER. III. model description and verification of parameter estimation codes," The Astrophysical Journal Letters **914**, L15 (2021).

[39] F. Özel, D. Psaltis, T. Güver, G. Baym, C. Heinke, and S. Guillot, "The dense matter equation of state from neutron star radius and mass measurements," The Astrophysical Journal **820**, 28 (2016).

[40] S. Tuna, K. Ünlütürk, and F. M. Ramazanoğlu, "Constraining scalar-tensor theories using neutron star mass and radius measurements," Phys. Rev. D **105**, 124070 (2022).

[41] R. Rosca-Mead, C. J. Moore, U. Sperhake, M. Agathos, and D. Gerosa, "Structure of neutron stars in massive scalar-tensor gravity," Symmetry **12** (2020), 10.3390/sym12091384.

[42] S. S. Yazadjiev, D. D. Doneva, and D. Popchev, "Slowly rotating neutron stars in scalar-tensor theories with a massive scalar field," Phys. Rev. D **93**, 084038 (2016).

[43] H.-J. Kuan, A. G. Suvorov, D. D. Doneva, and S. S. Yazadjiev, "Gravitational waves from accretion-induced descalarization in massive scalar-tensor theory," Phys. Rev. Lett. **129**, 121104 (2022).

[44] S. Bogdanov, C. O. Heinke, F. Özel, and T. Güver, "Neutron Star Mass-Radius Constraints of the Quiescent Low-mass X-ray Binaries X7 and X5 in the Globular Cluster 47 Tuc," Astrophys. J. **831**, 184 (2016), arXiv:1603.01630 [astro-ph.HE] .

[45] T. E. Riley *et. al.*, "A *NICER* view of PSR j0030+0451: Millisecond pulsar parameter estimation," The Astrophysical Journal **887**, L21 (2019).

[46] M. C. Miller *et. al.*, "PSR j0030+0451 mass and radius from *NICER* data and implications for the properties of neutron star matter," The Astrophysical Journal **887**, L24 (2019).

[47] T. E. Riley *et. al.*, "A *NICER* view of the massive pulsar PSR j0740+6620 informed by radio timing and XMM-newton spectroscopy," The Astrophysical Journal Letters **918**, L27 (2021).

[48] M. C. Miller *et. al.*, "The radius of PSR j0740+6620 from *NICER* and XMM-newton data," The Astrophysical Journal Letters **918**, L28 (2021).

[49] A. Bauswein, O. Just, H.-T. Janka, and N. Stergioulas, "Neutron-star radius constraints from GW170817 and future detections," Astrophys. J. Lett. **850**, L34 (2017), arXiv:1710.06843 [astro-ph.HE] .

[50] T. Dietrich, M. W. Coughlin, P. T. H. Pang, M. Bulla, J. Heinzel, L. Issa, I. Tews, and S. Antier, "Multimessenger constraints on the neutron-star equation of state and the Hubble constant," Science **370**, 1450–1453 (2020), arXiv:2002.11355 [astro-ph.HE] .

[51] E. Annala, T. Gorda, A. Kurkela, and A. Vuorinen, "Gravitational-wave constraints on the neutron-star-matter Equation of State," Phys. Rev. Lett. **120**, 172703 (2018), arXiv:1711.02644 [astro-ph.HE] .

[52] C. D. Capano, I. Tews, S. M. Brown, B. Margalit, S. De, S. Kumar, D. A. Brown, B. Krishnan, and S. Reddy, "Stringent constraints on neutron-star radii from multimessenger observations and nuclear theory," Nature Astron. **4**, 625–632 (2020), arXiv:1908.10352 [astro-ph.HE] .

[53] M. Corman, J. L. Ripley, and W. E. East, "Nonlinear studies of binary black hole mergers in einstein-scalar-gauss-bonnet gravity," Phys. Rev. D **107**, 024014 (2023).

[54] A. Hegade K. R., J. L. Ripley, and N. Yunes, "Where and why does einstein-scalar-gauss-bonnet theory break down?" Phys. Rev. D **107**, 044044 (2023).

[55] W. E. East and J. L. Ripley, "Dynamics of spontaneous black hole scalarization and mergers in einstein-scalar-gauss-bonnet gravity," Phys. Rev. Lett. **127**, 101102 (2021).

[56] J. Antoniadis *et al.*, "A Massive Pulsar in a Compact Relativistic Binary," Science **340**, 6131 (2013), arXiv:1304.6875 [astro-ph.HE] .

[57] P. Chen, T. Suyama, and J. Yokoyama, "Spontaneous scalarization: asymmetron as dark matter," Phys. Rev. D **92**, 124016 (2015), arXiv:1508.01384 [gr-qc] .

[58] S. Garcia-Saenz, A. Held, and J. Zhang, "Destabilization of black holes and stars by generalized proca fields," Phys. Rev. Lett. **127**, 131104 (2021).

[59] A. Coates and F. M. Ramazanoğlu, “Intrinsic pathology of self-interacting vector fields,” Phys. Rev. Lett. **129**, 151103 (2022).

[60] A. Coates and F. M. Ramazanoğlu, “Pervasiveness of the breakdown of self-interacting vector field theories,” Phys. Rev. D **107**, 104036 (2023).

[61] A. Coates and F. M. Ramazanoğlu, “Coordinate singularities of self-interacting vector field theories,” Phys. Rev. Lett. **130**, 021401 (2023).

[62] K. Clough, T. Helfer, H. Witek, and E. Berti, “Ghost instabilities in self-interacting vector fields: The problem with proca fields,” Phys. Rev. Lett. **129**, 151102 (2022).

[63] Z.-G. Mou and H.-Y. Zhang, “Singularity problem for interacting massive vectors,” Phys. Rev. Lett. **129**, 151101 (2022).

[64] L. Heisenberg, “A systematic approach to generalisations of general relativity and their cosmological implications,” Physics Reports **796**, 1–113 (2019), a systematic approach to generalisations of General Relativity and their cosmological implications.

[65] H. RUEGG and M. RUIZ-ALTABA, “The stueckelberg field,” International Journal of Modern Physics A **19**, 3265–3347 (2004), https://doi.org/10.1142/S0217751X04019755 .

[66] L. Annulli, V. Cardoso, and L. Gualtieri, “Electromagnetism and hidden vector fields in modified gravity theories: Spontaneous and induced vectorization,” Phys. Rev. D **99**, 044038 (2019).

[67] F. M. Ramazanoğlu, “Spontaneous tensorization from curvature coupling and beyond,” Phys. Rev. D **99**, 084015 (2019).

[68] J. a. M. S. Oliveira and A. M. Pombo, “Spontaneous vectorization of electrically charged black holes,” Phys. Rev. D **103**, 044004 (2021).

[69] E. Babichev, C. Charmousis, G. Esposito-Farèse, and A. Lehébel, "Hamiltonian unboundedness vs stability with an application to horndeski theory," Phys. Rev. D **98**, 104050 (2018).

[70] J. a. G. Rosa and S. R. Dolan, "Massive vector fields on the schwarzschild spacetime: Quasinormal modes and bound states," Phys. Rev. D **85**, 044043 (2012).

[71] J. S. Read, B. D. Lackey, B. J. Owen, and J. L. Friedman, "Constraints on a phenomenologically parametrized neutron-star equation of state," Phys. Rev. D **79**, 124032 (2009).

[72] R. Rosca-Mead, C. J. Moore, U. Sperhake, M. Agathos, and D. Gerosa, "Structure of neutron stars in massive scalar-tensor gravity," Symmetry **12**, 1384 (2020).

[73] J. R. Oppenheimer and G. M. Volkoff, "On massive neutron cores," Phys. Rev. **55**, 374–381 (1939).

[74] R. C. Tolman, "Static solutions of einstein's field equations for spheres of fluid," Phys. Rev. **55**, 364–373 (1939).

[75] K. Y. Ekşi, "Neutron stars: compact objects with relativistic gravity," Turk. J. Phys. **40**, 127–138 (2016), arXiv:1511.04305 [astro-ph.HE] .

[76] P. Haensel, A. Y. Potekhin, and D. G. Yakovlev, *Neutron stars 1: Equation of state and structure*, Vol. 326 (Springer, New York, USA, 2007).

[77] V. A. Urpin and D. G. Yakovlev, "On the growth of temperature within neutron stars," Astrophysics **15**, 429–433 (1979).

Appendix A

GHOST INSTABILITY IN MASSLESS VECTOR-TENSOR THEORY

When we have a vector field without a mass, i.e., $m_V = 0$, the Eq. (4.8) becomes

$$\hat{z} = -4\pi\beta\mathcal{A}^4\tilde{T} = -4\pi\beta\mathcal{A}^4(3\tilde{p} - \tilde{\epsilon}) \tag{A.1}$$

where $\tilde{p}$ is the pressure, and $\tilde{\epsilon}$ is the energy density in the Jordan frame, as in previous sections. Notice that $\hat{z}$ is zero outside the star and negative somewhere inside; hence in principle, it may never cross zero. In this case, The surface of the neutron star is where the first instance of the divergence in the field equations occurs. To see this consider the following TOV equation relevant to our discussion [73, 74]

$$\frac{\mathrm{d}\tilde{p}}{\mathrm{d}r} = -\frac{\tilde{\epsilon}\mu}{r^2}\left(1 + \frac{\tilde{p}}{\tilde{\epsilon}}\right)\left(1 + \frac{4\pi\tilde{p}r^3}{\mu}\right)\left(1 - \frac{2\mu}{r}\right)^{-1}. \tag{A.2}$$

Close to the surface, we have $\tilde{p} \ll \tilde{\epsilon}$ and $4\pi\tilde{p}r^3 \ll \mu$ [75, 76]. Hence, with the approximation $\tilde{\epsilon} \approx \tilde{\rho}$, this equation can be written in the following form

$$\frac{\mathrm{d}\tilde{p}}{\mathrm{d}\varrho} = -\tilde{\rho}\,\mathrm{g}, \tag{A.3}$$

where we introduced a new radial coordinate ϱ and local gravitational acceleration g as

$$\frac{\mathrm{d}\varrho}{\mathrm{d}r} = (1 - 2\mu/r)^{-1/2} \tag{A.4}$$

$$\mathrm{g} = \frac{\mu}{r^2}(1 - 2\mu/r)^{-1/2}. \tag{A.5}$$

We can approximate the metric (4.10) to Schwarzchild near the surface, namely, $\mu \approx M$ and $\nu \approx \ln(1 - 2M/R)$ with M as the mass and R as the radius of the star [77]. Then, defining a local proper depth $\widehat{r}$

$$\widehat{r} = (R - r)(1 - 2M/R)^{-1/2} \tag{A.6}$$

which makes the Eq. (A.4) take the form

$$\frac{\mathrm{d}\tilde{p}}{\mathrm{d}\widehat{r}} = \mathrm{g}_s \tilde{\rho}, \tag{A.7}$$

which is the equation describing a plane-parallel atmosphere that takes into account relativistic-corrected surface gravity $\mathrm{g}_s = \mathrm{g}(R) = (M/R)(1-2M/r_s)^{-1/2}$. This equation can be solved exactly for the outermost layers giving $\tilde{\rho} \propto \widehat{r}^{3/2}$ and $\tilde{T} \propto -4\pi\beta\widehat{r}^{3/2}$. This means that $\nabla_\mu \ln|\hat{z}|$ and the effective mass have divergent behavior near the surface.